

## A scattering function for correlated lamellae

Michael Camara<sup>a,1</sup>, Kabir Rishi<sup>a,b,1</sup>, Gregory Beaucage<sup>a,\*</sup>, Sathish K. Sukumaran<sup>c</sup>

<sup>a</sup> Chemical and Materials Engineering, University of Cincinnati, Cincinnati, OH, 45221, USA

<sup>b</sup> Centers for Disease Control and Prevention, National Institute for Occupational Safety and Health, Cincinnati, OH, 45213, USA

<sup>c</sup> Graduate School of Organic Materials Science, Yamagata University, 4 Chome-3-16 Jonan, Yonezawa, Yamagata, 992-8510, Japan

### ABSTRACT

Melt crystallized polymers display an emergent, multi-hierarchical, ordered structure made up of stacked lamellar single crystals that form fibrous or other meso structures which, in turn, form macroscopic crystallites. A dominant feature of small-angle scattering from these complex assemblies is a correlation peak associated with the stacking period. A new model-based function is proposed for small-angle scattering data from such correlated lamellar multi-hierarchical structures. Generally, routine use of scattering data has been limited to a 1-d analysis to determine the long period from Lorentz corrected data ( $I(q)q^2$  versus  $q$ ). Fourier transforms of the data are sometimes used to determine the 1-d pairwise correlation function for the electron-density distribution which has been further analyzed in terms of the structure of these materials. A simple 1-d fitting model limited to infinite width 2-d sheets was introduced by Hermans (1944; Hosemann, 1950) [1,2] in the 1940s with some success. A new approach, the Unified Born-Green Function (UBG), is proposed that uses the Unified Function as adapted to correlated lamellar structures and incorporates a Born-Green description of one-dimensional correlations. The UBG fit allows quantification of the average lamellar aspect ratio, the local degree of crystallinity within a stack, quantification of the stacking versus non-stacking amorphous, and two types of disorder in addition to the stacking period and lamellar thickness. UBG can account for higher levels of structure such as crystalline domains in block copolymers and convoluted lamellar structure. The UBG fit is compared to the Hermans (1944; Hosemann, 1950) [1,2] and a hybrid-Hermans function. Fits to data sets from a wide range of polyethylene are shown ranging from molecular weight standard samples that are isothermally crystallized, to commercial HDPE quenched from the melt and a metallocene blown film sample. Several other examples from the literature are explored. It is shown that the Unified fit allows for new understanding of the impact of thermal and mechanical history, chain structure, fillers, nucleating agents, and additives on the crystalline structure and the resulting physical properties. Limitations of the UBG approach are noted.

### 1. Introduction

Melt crystallized, semi-crystalline polymers form chain-folded, lamellar crystallites in a complex multi-hierarchical structure, that is, having many structural levels. At moderate degree of crystallinity (>40%) lamellae correlate into stacked bundles composed of alternating crystalline and amorphous layers. Often these stacked bundles are further organized into fibrillar structures that can radiate from a central nucleation site to form impinging spherulitic structures, and other complex hierarchies. Between fibrillar bundles, so called interfibrillar amorphous regions can form a significant volume fraction of the semi-crystalline polymer as can larger size inter-spherulitic amorphous regions [1–3]. This paper focuses on the nano-structural, stacked-lamellar level of morphology in these complex materials. On first observation these seem to present a simple structure from which a scattering function could be calculated to directly fit small-angle scattering data, Fig. 1, as was done by Hermans [4,5] in the 1940s.

#### 1.1. Gaussian fits to Lorentz corrected data

At high lamellar packing density, one-dimensional correlation in the thickness direction (normal to the lamellar surface) is observed associated with lamellar stacking, as shown in Fig. 1(b) and (d). This one-dimensional correlation of thicknesses is manifested at sizes larger than the thickness but usually smaller than the lateral dimensions of the lamellae so that the correlation or long-period peak falls in the two-dimensional scaling regime,  $I(q) \sim q^{-2}$ , associated with the large-scale structural level for lamellae (where  $q = (4\pi/\lambda)\sin(\theta/2)$ ,  $\lambda$  is the wavelength,  $\theta$  is the scattering angle, and  $I(q)$  is the scattered intensity). The lamella is a two-dimensional object, the form factor of which displays a dimensionality of 2 between the lateral size of the lamellae and the thickness. At high- $q$  the form factor displays Porod surface scattering and at low- $q$  the form factor displays a plateau reflecting point scattering since the dimensionality is no longer resolved. The structure factor impacts only the lamellar thickness direction since the lamellae do not correlate laterally. For this reason, the correlations can more easily be resolved by a Lorentz correction plot of  $I(q)q^2$  versus  $q$  [7–9]. The power

\* Corresponding author.

E-mail address: [gbeaucage@gmail.com](mailto:gbeaucage@gmail.com) (G. Beaucage).

<sup>1</sup> Equal contribution by authors.

of the scattering vector reflects the dimension of the object and is appropriate in the regime of  $q$  where that dimensionality is displayed. For lamellae it is appropriate between the thickness and the lateral size. Since the correlation peak occurs at sizes larger than the thickness it would seem to be appropriate to apply the Lorentz correction to obtain a Gaussian correlation peak [10,11]. The Lorentz correction removes the two-dimensional lamellar scaling and allows for a direct fit of the one-dimensional correlation peak or long period. One problem associated with this approach is that the Lorentz correction of scattering data can make a correlation peak appear even when the original scattering data do not display a clear correlation peak since the highest- $q$  data typically display a Porod decay of  $-4$  power-law slope while the lowest- $q$  data often display a weaker power-law decay, shallower than a  $-2$  decay, possibly associated with fibers. Further, it is often observed that higher order peaks associated with the Lorentz corrected data do not follow a strict integral order  $q$  value, i.e. first order should occur at  $q^* = 2\pi/\xi$  and second order at  $2q^*$  [12–14]. Fitting a Gaussian function to the Lorentz corrected data does not immediately resolve the lamellar thickness since only the stacking period, that includes both amorphous and crystalline regions, is measured. Since there are at least three distinct locations for the amorphous fraction in a semi-crystalline polymer, multiplication of the long period by the bulk volume fraction crystallinity from diffraction, density, or calorimetry might be less than quantitative for an approximation of the lamellar thickness. These issues have been partially resolved, for instance, by incorporation of more sophisticated descriptions of disorder in lamellar stacks. Although

indirect Fourier transforms of the scattering intensity,  $I(q)$  [15], and fits to the Lorentz-corrected scattering data [16–18] have been used to determine the lamellar structure, few attempts at directly fitting  $I(q)$  [19] have been made. The simple structural model proposed here might better serve as an analytical approach. The Unified Function allows for expansion of the fit to higher order structures such as crystalline domains, as shown for block copolymer resins at the end of this paper, or for fibrous or spherulitic structures. Such an expansion is not possible using the Lorentz correction or a correlation function analysis.

In addition to peak fits to the Lorentz corrected data, it is common to calculate the electron density correlation function for lamellar stacks by Fourier transformation of small-angle scattering data under approximations associated with extrapolation of the scattering pattern at low and high- $q$  [8,10,20–31]. This approach has led to significant success in determination of structural features and electron-density profiles for lamellar stacks as well as a description of the lamellar interfacial region. A disadvantage of a detailed analysis of transformed data from imperfectly correlated structures involves insufficient experimental  $q$ -range for the requisite extrapolation as well as assumptions involved in the extrapolation procedure. Additionally, due to the disconnect between the transform and the original data set, there exists the potential to misinterpret features in the scattering pattern that might more clearly be resolved as related to specific structural features in the original scattering pattern such as fibers or large-scale domains. In comparison, a direct fit to the original scattering data offers the potential of associating specific model parameters with specific features observed in scattering.

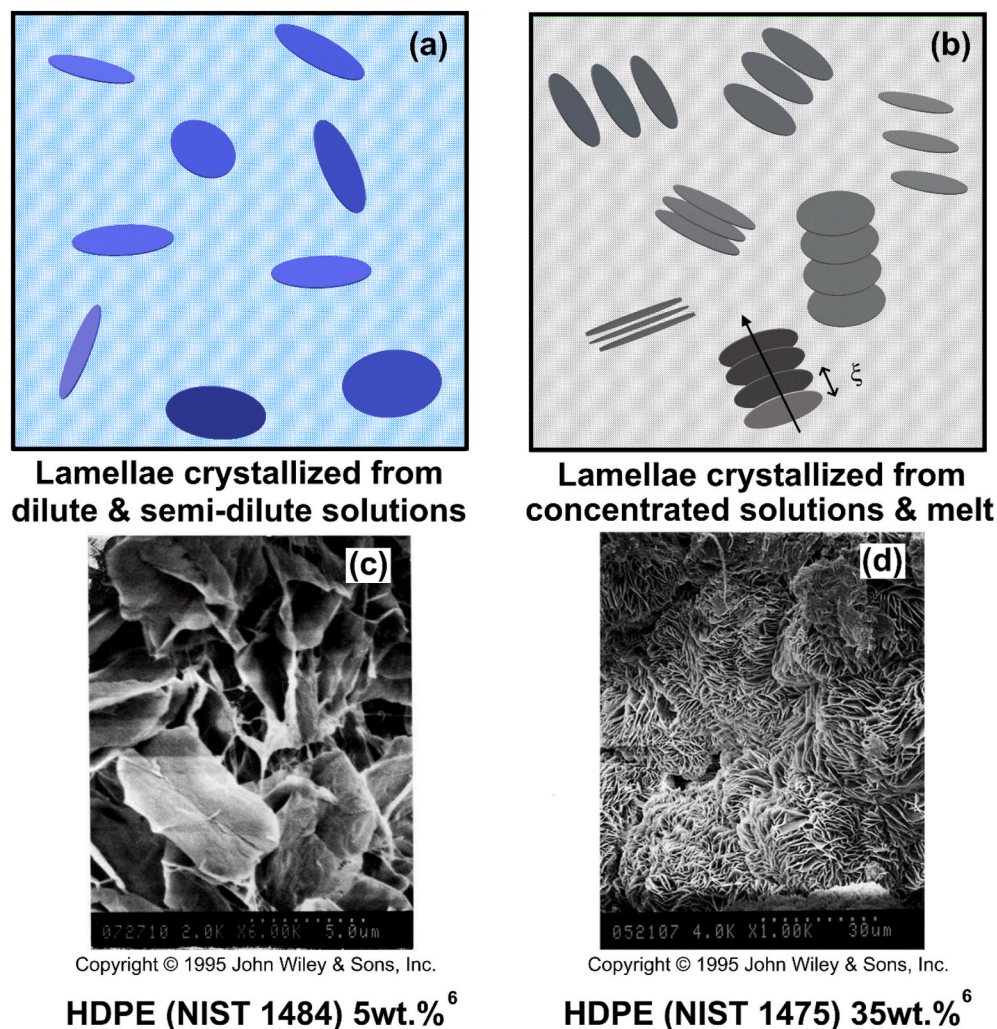


**Fig. 1.** (a) Schematic model of uncorrelated lamellae crystallized from semi-dilute to dilute solutions; (b) Schematic model of 1-d correlated (along the normal to the lamellae surface indicated by the arrow) lamellae crystallized from concentrated solutions/polymer melt with a high degree of crystallinity. Note that the stacks of circular lamellae in (b) are randomly oriented, and the long period,  $\xi$ , is exaggerated. (c) (d) TEM micrographs showing the dependence of crystalline structure on concentration for HDPE standard reference material 1484 in supercritical solution reproduced with permission from Pradhan, D. and Ehrlich, P. (1995), Morphologies of microporous polyethylene and polypropylene crystallized from solution in supercritical propane. *J. Polym. Sci. B Polym. Phys.*, 33: 1053–1063. <https://doi.org/10.1002/polb.1995.090330709> Copyright © 1995 John Wiley & Sons, Inc [6]. (c) uncorrelated lamellae crystallized from a 5 wt% semi-dilute solution and (d) randomly oriented correlated lamellae from a 35 wt% concentrated solution.

In any case, the different analytical techniques available for interpretation of small-angle scattering from melt-crystallized, semi-crystalline polymers are not exclusive and the direct fitting approach presented in this paper is intended as a potential alternative, or complement, to fitting of the Lorentz corrected data and to analysis of correlation functions.

### 1.2. The Hermans Function (HF)

Hermans obtained an expression for scattering from perfectly aligned, regularly spaced, and infinitely wide stacked lamellar sheets that are independently polydisperse in thickness of the crystalline and amorphous layers [4,5,32–37]. By assuming that the crystalline and amorphous thicknesses of the lamellae follow a Gaussian distribution and applying a Fourier transform, the absolute scattered intensity of a lamellae is,

$$I_{\text{HF}}(q) = \left(\frac{B_1}{q^4}\right) \text{Re} \left\{ \frac{(1 - H_L(q))(1 - H_a(q))}{1 - H_L(q)H_a(q)} \right\} \quad (1)$$

where  $q$  is the scattering vector,  $B_1$  is the Porod prefactor for the surface scattering in the high- $q$  regime assuming a smooth interface with  $I(q) = B_1 q^{-4}$ ,  $\text{Re}$  represents the real portion of the calculation for the complex functions,  $H_L(q) = \exp(it_L q - \{\sigma_L^2 q^2/2\})$  and  $H_a(q) = \exp(it_a q - \{\sigma_a^2 q^2/2\})$ . At low- $q$ , eq (1) describes a power law  $-2$  reflecting infinitely wide lamellae with  $I(q) = B_2 q^{-2}$ .  $H_L(q)$  depends on the mean thickness,  $t_L$ , and the standard deviation,  $\sigma_L$ , of the crystal portion of the lamellar stack, while  $H_a(q)$  depends on the mean thickness,  $t_a$ , and the standard deviation,  $\sigma_a$ , of the amorphous region between lamellae. The sum of the mean thicknesses of the amorphous and crystalline regions gives the mean long period of the lamellar stack with a standard deviation of the square root of the sum of the two variances. This formalism assumes that the standard deviation for lamellar and amorphous size (thickness) are independent parameters. The HF describes the surface scattering Porod region at high- $q$ , the Guinier region for the lamellar thickness, the structure factor for stacking of lamellae, and the two-dimensional scaling regime for infinite width lamellae. The function does not describe the lateral extent of the lamellae or higher order structures such as fibrous stacks and meso-structures such as spherulites. The Igor® code for HF is given in SI.

### 1.3. A hybrid Hermans/Unified Function (HHF)

The Unified Function (UF) breaks down complex scattering patterns as a function of reciprocal space vector,  $q = (4\pi/\lambda)\sin(\theta/2)$ , into hierarchical structural levels [38–40], such that

$$I_{\text{UF}}(q) = \sum_{i=1}^n \left[ G_i \exp\left(\frac{-q^2 R_{g,i}^2}{3}\right) + B_i (q_i^*)^{-P_i} \exp\left(\frac{-q^2 R_{g,i-1}^2}{3}\right) \right] \quad (2)$$

where  $q_1^* = q[\text{erf}(kqR_{g,i}/\sqrt{6})]^{-3}$ , with  $k = 1.06$  for  $1 \leq P_i < 3$  and  $k = 1$  for  $P_i > 3$ . A structural level, from a scattering perspective, is composed of a Guinier regime (prefactor,  $G_i$  and size  $R_{g,i}$ ) in the first term, and an associated power-law regime (prefactor,  $B_i$  and structure,  $P_i$ ) in the second term [38–40]. The subscript "i" reflects the index of the structural level that is numbered from the smallest size (highest- $q$ ) to the largest size. The UF was derived to account for the limit of power-law regimes at low- $q$  near the associated Guinier regime and can reproduce many conventional scattering functions such as the Debye function for Gaussian polymer coils and calculations for polydisperse spheres in a universal manner with the minimum number of free parameters. It has recently been shown by Vogtt et al. [41] that local structural scattering functions such as the HF can be used in the UF to account for higher-level features, such as the lateral limit of lamellar width and length and possible fibrillar and mesoscopic structures at larger sizes. The HF describes infinitely wide stacked lamellae which display a

power-law  $-2$  at low- $q$ . To limit this power-law at the lamellar lateral extent, a Guinier function that accounts for the lamellae size,  $R_g$ ,  $2 = \sqrt{\{(R^2/2) + (t^2/12)\}}$ , that reflects both the lateral size,  $D = 2R$ , and the thickness,  $t$ , of the lamellae, as discussed later [42], can be added to a modified HF based on the Unified approach to yield a hybrid-Hermans function (HHF). In fact, higher structural levels can be added to account for fibrillar or spherulitic structures. For a three-level structure composed of lamellar thickness ( $i=1$ ), the lateral size ( $i=2$ ), and a meso-structure such as fibers or other clusters of lamellar stacks ( $i=3$ ) the hybrid-Hermans function (HHF) for scattering intensity can be expressed as,

$$I_{\text{HHF}}(q) = \left[ G_3 \exp\left(\frac{-q^2 R_{g,3}^2}{3}\right) + B_3 (q_3^*)^{-P_3} \exp\left(\frac{-q^2 R_{g,2}^2}{3}\right) + G_2 \exp\left(\frac{-q^2 R_{g,2}^2}{3}\right) + I_{\text{HF}}(q_2^*) \right] \quad (3)$$

where  $q_2^* = q[\text{erf}(1.06qR_{g,2}/\sqrt{6})]^{-3}$ ,  $q_3^* = q[\text{erf}(1.06qR_{g,3}/\sqrt{6})]^{-3}$  and "erf" is the error function [38–40]. Here the last term is the HF that accounts for the first, smallest structural level of correlated lamellar thicknesses, as well as a 2-d level scaling regime so that the last term in eq (3) would extend to  $q \Rightarrow 0$  with a power-law slope of  $-2$ . To terminate this power-law at the lamellar width,  $q_2^*$  is used which limits the power-law at  $R_{g,2}$  for the overall lamellar size (including the lamellar width). The Guinier regime for the overall lamellar size (lamellar width) is added to account for the Guinier regime below the  $-2$  slope power-law. The first two terms (and further terms which could be added) account for the hierarchical structure in the normal way used in the Unified Function. The Igor® code for HHF is given in SI.

### 1.4. Proposed Unified-Born Green Function (UBG) for lamellar scattering

#### 1.4.1. The Unified Function for uncorrelated lamellae

We have previously developed a simple scattering function for isolated, uncorrelated lamellae [42] crystallized from semi-dilute to dilute solutions to produce semi-crystalline polymer foams through supercritical solvent extraction in the absence of surface tension [42]. Under dilute and semi-dilute conditions, lamella do not significantly correlate [6,43], as shown in Fig. 1(a) and (c), so that modeling of small-angle scattering from these systems is a less challenging problem. The nano-scale scattering from polydisperse uncorrelated lamellae,  $I_0(q)$ , can be fit through the UF, eq (2), truncated to the first two structural levels ( $n=2$  in eq (2)) corresponding to the lamellar thickness and the lateral size of lamellae as discussed previously. These two structural levels are associated in the UF for lamellae since the two-dimensional level terminates in or is "limited" by the thickness level [39,40,42],

$$I_0(q) = G_2 \exp\left(\frac{-q^2 R_{g,2}^2}{3}\right) + B_2 (q_2^*)^{-2} \exp\left(\frac{-q^2 R_{g,1}^2}{3}\right) + G_1 \exp\left(\frac{-q^2 R_{g,1}^2}{3}\right) + B_1 (q_1^*)^{-4} \quad (4)$$

Note that for  $i=0$ ,  $R_{g,0}=0$  indicates no high- $q$  cutoff or termination to the level 1 Porod power-law decay. Since,  $P_1=4$  and  $P_2=2$ , as discussed previously, the remaining six parameters ( $G_1, G_2, B_1, B_2, R_{g,1}$  and  $R_{g,2}$ ) in eq (4) can be expressed in terms of only the lamellar thickness,  $t$ , the average lateral size of a lamellae (average of the width and length),  $R$ , and the contrast factor,  $G_1$ . For example,  $R_{g,1} = t/2$  (from equation 41, p. 28 in Ref. [44]). Additionally,  $B_1 = 2\pi(G_2/V)(S/V) = G_1 \{(2R_{g,1} + R)/(R_{g,1}^4 R)\} = 16G_1 \{(t+R)/(t^4 R)\}$  [42], for a circular platelet with the surface area,  $S = 2\pi R(R+t)$ , and volume,  $V = \pi t R^2$ . For the two-dimensional regime,  $G_2, R_{g,2}$  and  $B_2$  were previously described for lamellae [42]:  $G_2 = G_1 (R/R_{g,1})^2 = G_1 (2R/t)^2$ , the overall radius of gyration for a circular platelet,  $R_{g,2} = \sqrt{\{(R^2/2) + (R_{g,1}^2/3)\}} = \sqrt{\{(R^2/2) + (t^2/12)\}}$ , and  $B_2 = 2G_2/R^2 = 2G_1/R_{g,1}^2 = 8G_1/t^2$  (Note that in Ref. [42],  $i=1$ , represents

that largest structural level, defined otherwise here).

One-dimensional correlation in melt-crystallized polymers present additional parameters, for instance the local volume fraction crystallinity within a stack of lamellae,  $\phi$ . In the proposed function, a maximum of six parameters are used to fit these complex structures. These parameters account for the average local structure (lamellar thickness and width), the packing (related to the local degree of crystallinity within a stack), the stacking repeat distance or long period, and structural disorders due to (i) misorientation and interfacial broadening, and (ii) stacking irregularity and finite stack size [24]. Through the use of a local fit to the Porod decay at high- $q$ , the number of parameters needed to fit these curves can be reduced to five as discussed below. By comparison the Hermans function [4,5] requires five parameters and the hybrid Hermans function limited to the lamellar width level (comparable in number of structural levels) requires seven parameters.

#### 1.4.2. Scattering function for correlated lamellae

Correlations are modeled through adoption of the Born and Green approximation (p. 46 of reference [44]),

$$I_{BG}(q) = \frac{I_0(q)}{1 + p A(q, \xi)} \quad (5)$$

where the form factor,  $I_0(q)$  is the scattered intensity in the absence of correlations, eq (4). In eq (5), correlations for  $I_0(q)$  include both level 1 (thickness) and level 2 (two-dimensional) since lamellae are “regular” objects in a fractal sense [45], that is, there is a fixed orthogonal relationship between the lamellar normal and the in-plane vector. This contrasts with the 1-d correlation of the HF.  $A(q, \xi)$  is an amplitude function which describes the interference due to correlations with a long period or correlation distance of  $\xi$  and  $p$  is a packing factor directly related to the second virial coefficient for non-interacting, hard-core domains. In the most general case [44] of structures spherically correlated in 3-dimensions,  $A(q, \xi)$  is the amplitude function for a sphere [46] and  $p=8(V_0/V_{total})$  where  $8V_0$  is the excluded volume shared by two hard-core spheres each of volume  $V_0$  and  $V_{total}$  is the volume available to the sphere as described by Guinier and Fournet [44]. For correlated lamellar sheets, both  $p$  and  $A(q, \xi)$  are modified from this general case of spherical correlations. The one-dimensional amplitude function,  $A(q, \xi)=\sin(q\xi)/q\xi$ , for 1-d correlations is used in eq (4), as was previously given, for instance, by Porod [47]. This amplitude function must be averaged for random orientations of the lamellar stacks (under an assumption of isotropic scattering) using a cosine integral,

$$\int_0^{\pi/2} \{\sin(q\xi \cos\gamma)/(q\xi \cos\gamma)\} d\gamma, \text{ where } \gamma \text{ is the angle of integration for}$$

different orientations of the lamellar stacks with respect to the scattering experiment. The fitting routine using this one-dimensional correlation includes a numerical integration of  $A(q, \xi)$  to account for the random orientation of different lamellae stacks in the scattering volume (Supporting Information).

#### 1.4.3. Packing of stacked lamellae

The packing factor,  $p$ , for correlated lamellae retains the definition as the ratio of the *excluded volume* to the *available volume* [44]. The excluded volume for lamellae is defined as,  $2(D/t)^2V$ , where  $D=2R$  is an average lateral diameter for a lamella,  $t$  is the lamellar thickness and  $V=\pi tR^2=2\pi R_{g,1}R^2$  is the occupied volume per lamella. The available volume is given by  $V_{total}=V/\phi$ , where  $\phi$  is the local degree of crystallinity within a lamellar stack.  $\phi$  can be larger than the bulk volume fraction crystallinity due to segregation of lamellar stacks in the bulk sample, that is, in addition to inter-lamellar amorphous, the bulk sample contains inter-fibrillar and inter-spherulitic amorphous components. This local volume fraction crystallinity is equal to the ratio of the lamellar thickness to the correlation distance,  $\phi=t/\xi=2R_{g,1}/\xi$ , so,

$$p = 2 \left( \frac{D}{t} \right)^2 \phi = 2 \left( \frac{R}{R_{g,1}} \right)^2 \left( \frac{2R_{g,1}}{\xi} \right) = \frac{4R^2}{R_{g,1}\xi} \quad (6)$$

The local volume fraction crystallinity, estimated directly from the scattering curve as described above, can be compared with calorimetric bulk measurements to give an indication of the extent of amorphous material not associated with lamellar stacks or, equivalently, the extent of segregation of lamellar stacks. The average diameter of the lamellae,  $D$ , can be obtained from the packing factor,  $p$ , using eq (6) and should be much larger than  $t$  in most cases. The aspect ratio,  $A=D/t=2R/t$  and for the melt-crystallized polyethylene samples investigated in this study,  $A$  is about 7. Note that it is assumed that the lamellae display lateral symmetry to simplify the fit. This is not necessary and lateral asymmetry could be accounted for through a more elaborate fit using a parallel approach and introducing one additional parameter. For the samples studied here this might be necessary for only one case, Equistar BS H.

#### 1.4.4. Orientational and interfacial disorder in stacked lamellae

Debye-Waller disorder for 3-d crystals is associated with random thermal motion of atoms about their lattice placement. Long-range order is retained but about this perfect long-range order there is vibrational motion. This is modeled through the introduction of a Gaussian term that results in a dampening of the higher order peaks at high- $q$ . The Debye-Waller factor is a general disorder term commonly used in diffraction, scattering and reflectivity. The Debye-Waller factor [48] introduces a separate fitting parameter,  $k_l$ ,

$$I_{mod\ BG}(q) = \frac{I_0(q)}{1 + p A(q, \xi) \exp(-q^2 \xi^2 k_l)} \quad (7)$$

For lamellae, the Debye-Waller factor could account for misalignment of the lamellae in terms of the lamellar normal while retaining long range order. The Debye-Waller factor could also be related to the electron density profile normal to the lamellae associated with several features such as chain folding at the interface and continuity of polymer chains from the dense crystalline phase to the amorphous phase. Accounting for the Debye-Waller factor in eq (7) results in better appearance to the fits since damped, high-angle correlation peaks are correctly represented.  $k_l=0$  indicates the absence of the Debye-Waller effect. (This might be expected in conjunction with a high degree of local crystallinity within a stack.) Typical values for  $k_l$  are on the order of 0.01–0.05 for the samples investigated in this study.

#### 1.4.5. Irregular periodicity and finite crystals

For lamellar stacking, variability in the stacking period, that is, more crowded lamellae in one region versus another, is a type of long-range disorder. Additionally, the finite number of lamellae in each stack is the ultimate type of long-range disorder to the stacking repeat. Due to long-range disorder, the second order peak which results from diffraction from lamellar stacking does not always occur at exactly  $2q^*$ , where  $q^*$  is the  $q$  position of the first peak [14]. This long-range distortion of the lattice is resolved by a factor that accounts for irregular periodicity,  $\delta$ , such that  $q$  is replaced by  $q_{mod}=q \exp(\delta\{q-(2\pi/\xi)/q\})$  [46]. To account for the long-range distortion of the lattice such as due to finite crystals or variability in the correlation distance,  $q_{mod}$  replaces  $q$  in the structure factor part of eq (9). (Examples of this type of distortion are shown later in the Results section, Fig. 3(a)). The function is chosen so that when  $\delta=0$ , the stacking perfectly repeats over long distances. When a second order peak is not observed,  $\delta$  should be fixed at 0 since this type of disorder cannot be quantified.

Disorder in the stacking and the presence of a finite number of lamellae in a stack (Scherrer-type broadening) is accounted for by  $\delta$ . When  $q=2\pi/\xi$ ,  $q_{mod}=q$ , but above the peak,  $q>2\pi/\xi$ ,  $q_{mod}>q$ , and below the peak,  $q<2\pi/\xi$ ,  $q_{mod}<q$ .  $\delta$  accounts for a shift of high-order peaks to higher values of  $q$  as observed in the data. It is possible to mathematically link  $\delta$  and the Scherrer equation by associating the shift in  $q$  above

and below the peak with the peak breadth. The advantage of the  $\delta$ -function is that it can be used in the structure factor for direct fitting of the scattering data. Typical values for  $\delta$  are on the order of 0–0.1 which indicates that either the stacking is regular (0), or some stacking irregularity exists (0.1).

Small angle X-ray scattering (SAXS) data from melt-crystallized polyethylene of variable degree of crystallinity were fit using the Unified Born-Green function (UBG) with 1-d correlations in eq (8),

$$I_{\text{UBG}}(q) = I_0(q) \left\{ 1 + p \left( \int_0^{\pi/2} \frac{\sin(q_{\text{mod}} \xi \cos \gamma)}{q_{\text{mod}} \xi \cos \gamma} d\gamma \right) \exp(-q_{\text{mod}}^2 \xi^2 k_1) \right\}^{-1} \quad (8)$$

For  $I_0(q)$  in eq (4),  $R_{g,1}$  and  $B_1$  (instead of  $G_1$ ) are used as fitting parameters because  $R_{g,1}$  is directly related to the lamellar thickness, and the Porod constant,  $B_1$  can be fixed by a local fit at high- $q$  in most cases. From eq (6),  $R = \sqrt{(p\xi R_{g,1}/4)}$  is obtained from the packing factor,  $p$ , as a fitting parameter since  $p$  is directly observed in terms of the shape and strength of the correlation peak. The remaining *three* fitting parameters in the UBG function, eq (8), are the correlation distance ( $\xi$ ), interfacial broadening parameter ( $k_1$ ) and stacking irregularity factor ( $\delta$ ). In many cases  $\delta$  is effectively 0 and can be removed from the fit by holding it at 0, e.g., when there is no second order peak. Usually,  $B_1$  is fixed in the fit to a local fit value obtained from a Porod power-law of  $-4$  slope at high- $q$  reducing the number of fit parameters in eq (8) by one. Thus, the Unified Born-Green function (UBG) will involve *four* or *five* free parameters depending on the presence or absence of a strong second order peak. The Igor® code for the UBG is given in the Supporting Information. The model proposed in eq (8) assumes that 1) the lamellae are laterally symmetric and have a platelet structure; 2) there are only two contrasts in the system, amorphous and crystalline, that is, the interlamellar amorphous contrast is the same as the interstack/interfibrillar/inter-spherulitic amorphous contrast. The contrast between a lamellar stack and the amorphous region is not explicitly described but it can be added as a further structural level as is demonstrated with semi-crystalline block copolymers at the end of the Results section.

Additional structural levels can be added to UBG, eq (8), like the HHH in eq (3) to yield a modified UBG such that,

$$I_{\text{mod UBG}}(q) = I_{\text{UBG}}(q) + G_3 \exp\left(\frac{-q^2 R_{g,3}^2}{3}\right) + B_3 (q_3^*)^{-4} \exp\left(\frac{-q^2 R_{g,\text{cut-off}}^2}{3}\right) \quad (9)$$

Here,  $q_3^* = q[\text{erf}(qR_{g,3}/\sqrt{6})]^{-3}$  as discussed previously and  $R_{g,3}$  represents the radius of gyration of the domains. Notice that the prefactor of 1.06 is missing from  $q_3^*$  since this structural level involves surface scattering from the domains,  $P_3=4$  [39,40]. Additionally, note that in the second part of eq (9), the overall radius of gyration of the lamellae platelets,  $R_{g,2}$ , is replaced by  $R_{g,\text{cut-off}}$  to improve the fit [38,39].

**Table 1**

Details of various polyethylene grades investigated in this study. The bulk degree of crystallinity,  $\phi_{\text{DSC}}$  and the melting temperature,  $T_m$ , were determined from DSC measurements.  $M_w$  and  $\frac{M_w}{M_n}$  are available from the product specifications while  $\rho$  is the nominal density.

Polyethylene	Source	$\phi_{\text{DSC}}$	$M_w$ (kg/mol)	$\frac{M_w}{M_n}$	$\rho$ (g/cm <sup>3</sup> )	$T_m$ (°C)	Preparation	Branching
SRM® 1482	NIST	0.85	13.6	1.19	–	132.9	120°C <sup>a</sup>	0 <sup>d</sup>
SRM® 1483	NIST	0.76	32.1	1.11	–	133.5	120°C <sup>a</sup>	0 <sup>d</sup>
SRM® 1484	NIST	0.60	119.6	1.19	–	133.0	120°C <sup>a</sup>	0 <sup>d</sup>
LS6180	Equistar Chemicals LP	0.73	75	7.4	0.96	133.2	120°C <sup>a</sup>	–
Equistar BS A	LyondellBasell	0.68	148	9.6	0.96	128.7	RT <sup>b</sup>	4 <sup>d</sup> per 10000 <sup>e</sup>
Equistar BS H	LyondellBasell	0.67	150	8.9	0.96	129.1	RT <sup>b</sup>	0.5 <sup>d</sup> per 10000 <sup>e</sup>
Equistar 1	LyondellBasell	0.67	–	–	0.95	128	RT <sup>c</sup>	–
Metallocene, Exceed™ 399L60	ExxonMobil	0.35	144	2.7	0.93	120.1	Blown Film	110 <sup>f</sup> per 10000 <sup>e</sup>

<sup>a</sup>Isothermal crystallization. <sup>b</sup>Quenched at room temperature. <sup>c</sup>Crystallized at room temperature. <sup>d</sup>Number of long-chain branches. <sup>e</sup>Number of carbon atoms in the polymer backbone. <sup>f</sup>Number of short-chain branches.

## 2. Experimental

### 2.1. Sample preparation

The high-density polyethylene (HDPE) samples used in this study are described in Table 1. Scattering samples were prepared in four ways. All three NIST HDPE samples and the Equistar LS6180 commercial sample were isothermally crystallized in 2 mm thick plaques at 120 °C after being pressed in the melt between aluminum plates, Table 1 [49]. Equistar 1 was pressed into 1 mm plaques from the melt at 120 °C then cooled in a room temperature press between aluminum plates. The Equistar BS A and BS H samples were quenched from the melt in room temperature water in 2 mm plaques pressed in the melt between aluminum plates. The Metallocene 399L60 was prepared as a blown film at LyondellBasell's pilot plant in Cincinnati. For this blown film, the scattering sample was composed of about 20 layers of a 5 mil. thick blown film.

The samples give an indication of some of the variability in semi-crystalline structure that may be observed and demonstrate the effectiveness of the proposed model to discern such morphological variability. Generally, such variability is manifested in the large-scale features at low- $q$  and often reflect high extents of asymmetry for the lamellar structures such as in the Equistar BS A and BS H samples discussed in the Results section.

### 2.2. Small-angle X-ray scattering

Small-angle X-ray scattering (SAXS) measurements were made on a commercial 2-m pinhole SAXS camera made by Siemens (Bruker NANOSTAR™ system) which includes a 2-d wire detector of high resolution for NIST 1482, 1483, 1484 and Equistar LS6180 samples. The remaining samples, Equistar BS A, BS H and Metallocene 399L60, were measured on the Oak Ridge National Laboratory 10-m pinhole SAXS camera and on a Bense-Hart Camera at Argonne National Laboratory. Equistar 1 was measured on the combined SAXS/WAXS/USAXS instrument at beamline 9-ID C at Argonne National Laboratory. The diffraction data for Equistar BS A and BS H samples was recorded using an INEL 1-d diffractometer at the UNM/Sandia Scattering Center in Albuquerque, New Mexico. All scattering data were corrected for background and detector sensitivity using standard data correction procedures. Data from Oak Ridge and Argonne National Laboratories are in absolute intensity using secondary and primary standardization, respectively. The data from the Bruker instrument are in relative intensity.

### 2.3. Differential scanning calorimetry

DSC scans for all samples, except Equistar 1, were performed on a PerkinElmer DSC IV. The degree of crystallinity,  $\phi_{\text{DSC}}$ , in Table 1 was determined from the enthalpy of melting and a heat of fusion for perfectly crystalline PE of 288 J/g [49,50]. The melting point,  $T_m$ , was

determined by cooling the polyethylene from the melt at 150 °C at a rate of  $-5$  °C/min to 30 °C, then reheating at  $+10$  °C/min. The value reported in Table 1 is the peak value for the melting endotherm. For Equistar 1, a TA Instruments Q1000 DSC was used to find the crystallinity from the enthalpy of melting and melting point,  $T_m$ . To determine the melting point, the sample was loaded at 40 °C, cooled to  $-20$  °C at a rate of 10 °C/min, held for 5 min, then increased to 160 °C at a rate of 10 °C/min.

### 3. Results

#### 3.1. Comparing the traditional HF, the HHF and the modified UBG for HDPE

Fig. 2 shows the  $I(q)$  versus  $q$  curve for the Equistar 1 HDPE sample. This curve was fit to the literature HF (solid black curve, eq (1)), the proposed HHF (dashed blue curve, eq (3)), and the proposed modified UBG (solid green curve, eq (9)). Fig. 2 also shows the normalized residuals (right axis) for the HF, HHF, and modified UBG to the scattered intensity. Note that the calculated curve for the Unified Function with correlations removed (eq (4)) is shown by the dashed grey curve. This curve clearly shows the  $-4$  power-law slope at high- $q$  indicative of a smooth lamellar surface and a corresponding Guinier knee, whereas the intermediate  $q$  region shows a characteristic  $-2$  slope associated with the 2-d lamellae. Due to structural correlations, this structure is screened as evidenced in the  $I(q)$  versus  $q$  data (red circles). The literature HF, eq (1), can fit the primary peak at  $q^*$  but slightly misses the secondary peak at  $2q^*$  as evidenced by examining the normalized residuals in Fig. S1 in the Supporting Information. In Fig. S1 in the Supporting Information, the normalized residuals for the secondary peak for the UBG are closer to zero as opposed to the HF. Since the HF assumes infinite lamellar width, the data at intermediate- $q$  follows a slope of  $-2$  that extends to low- $q$ . Consequently, the HF fit would not have a level 2 Guinier knee. Additionally, the function uses an incorrect  $R_{g,1}$  cutoff for the lateral length of

the lamellae which leads to the function not being able to fully fit the primary peak and the subsequent low- $q$  region as shown in Fig. 2. Alternatively, the HHF can fit both the long period and low- $q$  region representing the higher-level structure of the stacked lamellae. The HHF can fit the secondary peak better than the HF, like the modified UBG, as shown in Fig. S1 in the Supporting Information. Combining the Unified function in the HHF allows for the calculation of the lateral size,  $R$ , of the lamellae, which cannot be found from the HF. Additionally, by appropriately fitting the low- $q$  slope associated with a lamellar superstructure, level 3, with a larger power-law slope, the simplifying assumptions in the HF can be rectified. However, a major drawback of both these functions is that the crystalline and amorphous parameters in  $H_1$  and  $H_2$  can be interchanged and still provide an identical fit to the long period. Further details of the crystal structure being analyzed need to be known or supplementary analysis carried out to be confident in the thickness distributions for the amorphous and crystalline portion of the lamellae. The HHF and HF give two Gaussian standard deviations for the crystalline and amorphous domains, but they do not yield details of the disorder as described by the interfacial broadening parameter ( $k_f$ ) and stacking irregularity factor ( $\delta$ ), which are found when using the UBG/modified UBG model.

The fit parameters for the HF and HHF can be found in Table 2. The average thickness and standard deviation of the amorphous phase,  $t_a$  and  $\sigma_a$  respectively, and the average thickness and standard deviation of the crystalline phase,  $t_L$  and  $\sigma_L$  respectively, are found from the fits which allows one to determine the average long period and the combined crystalline and amorphous standard deviation,  $\xi$  and  $\sigma_{L+a}$  respectively. The HF and the HHF yield similar phase thicknesses, but the standard deviation for the amorphous phase is much larger for the HHF compared to the HF due to the additional parameters in the HHF needed to accurately fit the low- $q$  portion of the scattering data. Where possible, error values are also given in Table 2 for each of the parameters.  $t_L$  and  $\sigma_L$  were held in the HHF fit. Comparing the error values amongst the different fits, we see they are all of the same magnitude, which allows reasonable

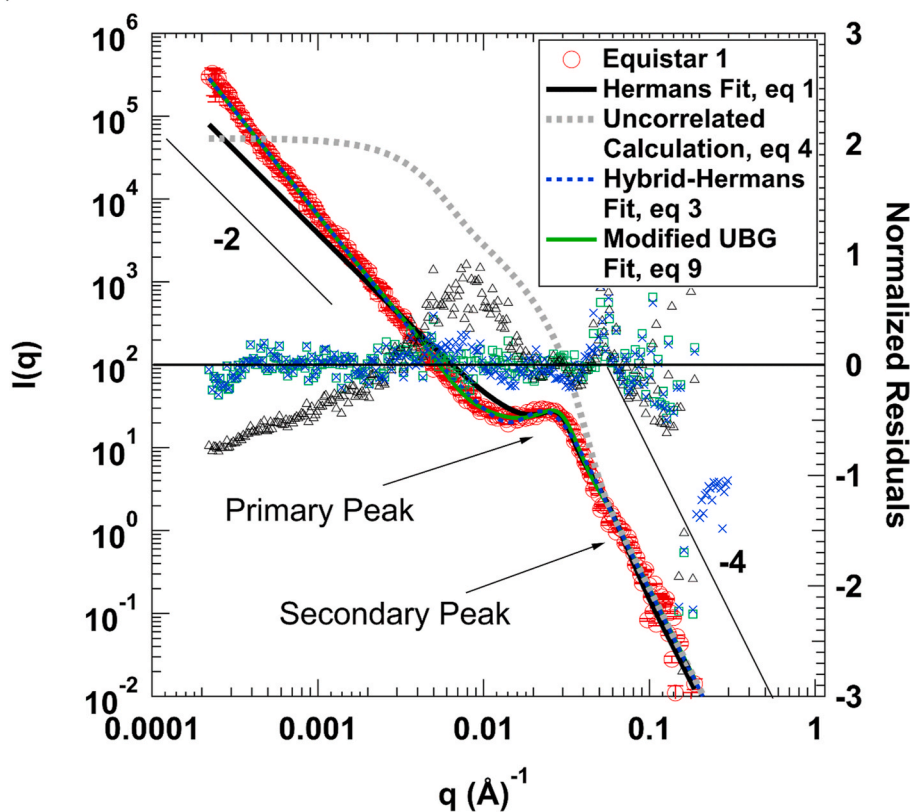
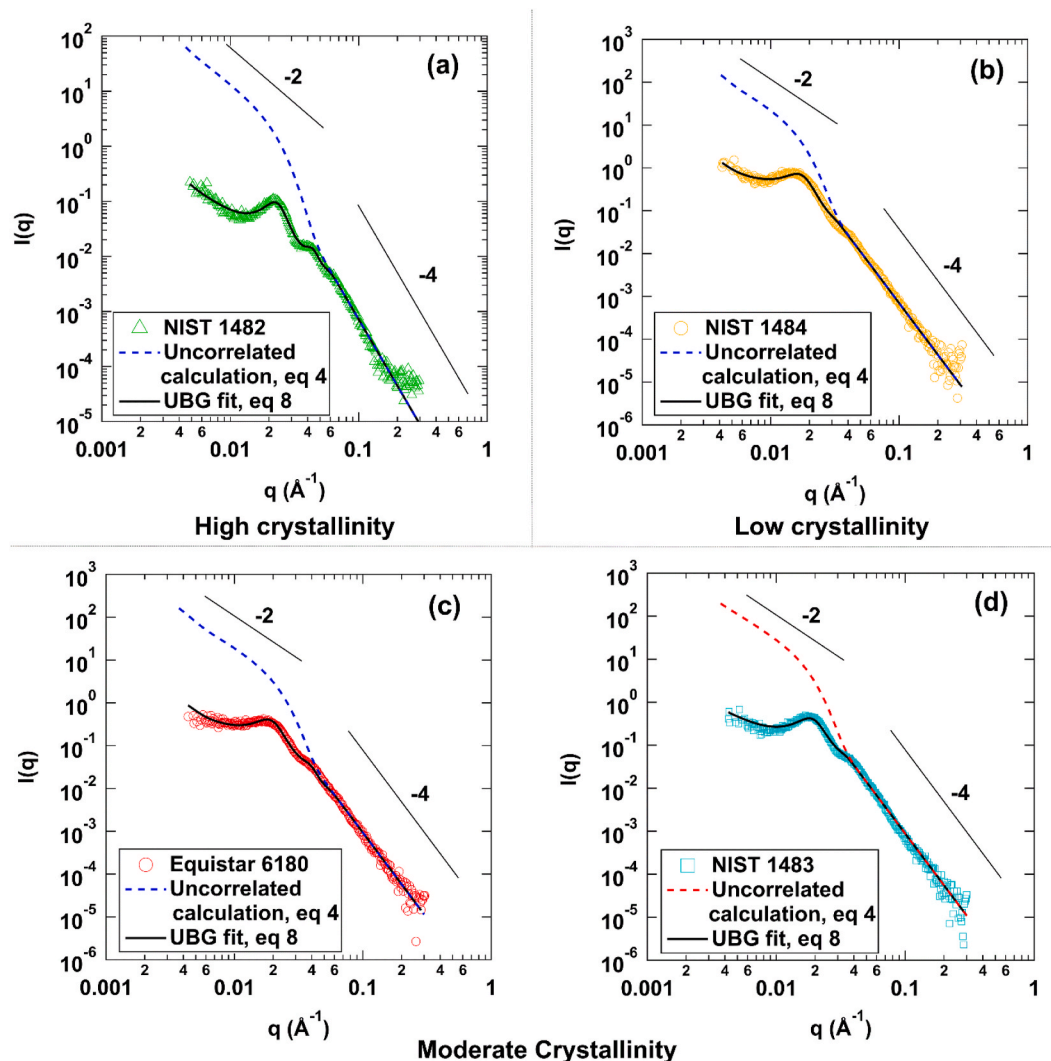


Fig. 2. USAXS curve,  $I(q)$  versus  $q$ , for Equistar 1 HDPE sample. The solid black line is the HF, eq (1), while the dashed blue line is the HHF, eq (3). The uncorrelated calculation, eq (4), is shown by the dashed grey line while the modified UBG, eq (9), is given by the solid green line. The normalized residuals (right axis),  $\{I(q) - I_{fit}(q)\}/I(q)$ , for each fit are shown by the corresponding-colored symbols. Note that the horizontal black line (no residuals read from the right axis) represents a perfect fit. (For interpretation of the references to color in this figure legend, the reader is referred to the Web version of this article.)



**Fig. 3.** SAXS curve ( $I(q)$  versus  $q$ ) for highly crystalline ( $\phi_{DSC}$  NIST 1482 (a); low crystallinity NIST 1484 (b); moderately crystalline Equistar 6180 (c) and NIST 1483 (d). The solid curve represents the proposed UBG in eq (8) whereas the dashed curve represents the calculated Unified fit in the absence of correlations using the fit parameters, eq (4).

**Table 2**

Fit parameters for Equistar 1 from eqs (1), (3) and (9) and calculated values for the melting temperature from Hoffman-Lauritzen theory [51]. (Errors are propagated from the counting errors.).

Fit	$t_a$ (Å)	$\sigma_a$ (Å)	$t_L$ (Å)	$\sigma_L$ (Å)	$\xi$ (Å)	$\sigma_{L+a}$ (Å)	$R_{g,1}$ (Å)	$R_{g,2}$ (Å)	$p$	$R$ (Å)	Calculated $T_{m,Hoffman}$ (°C) ( $T_{m,DSC}=128$ °C)
Hermans	47.5 (±0.1)	23.4 (±0.1)	146.2 (±0.4)	58.0 (±0.2)	193.7 (±0.4)	62.5 (±0.2)	–	–	–	–	116.5
Hybrid-Hermans	53 (±0.9)	47 (±0.6)	142.9 (±0.7)	65	195.9	80.2	71.5*	119.7	7.2*	158.9*	115.9
modified Unified Born Green	4.8 (±0.8)	–	185.0 (±0.7)	–	189.8 (±0.3)	–	92.5 (±0.4)	461.2	95.7 (±0.8)	647.9 (±2.9)	122.1

\* $R_{g,1}$ ,  $p$ , and  $RR$  calculated from  $R_{g,2}$  for the HHF.

comparison of the fits.

Differences between HHF and modified UBG values of  $R_{g,1}$ ,  $R_{g,2}$ ,  $p$ , and  $R$  are due to the assumption in the HHF calculation that the lamellae are uncorrelated. Also note the differences between the crystalline thicknesses of the lamellae from the different fits. While the long periods are similar across the different fits, the crystalline/amorphous split that makes up the long period is very different. UBG has the amorphous region being a very minor portion of the overall lamellae while the HF and HHF show the lamellae being made up of much more amorphous. Using

the Hoffman-Lauritzen theory [51] to calculate the melting temperature of a crystal from the thicknesses allowed comparison of the fits to the measured melting temperature seen by DSC, 128 °C. As shown in Table 1,  $T_{m,Hoffman}$  is most closely matched by the modified UBG. Given the better fit to the data and the more accurate prediction of the melting temperature, eq (9) can be used to model the polymers samples to yield not only accurate lamellae thickness, but also give insight into the lateral size, lamellae disorder, and long-range order of the crystal structure where the HF and HHF cannot.

### 3.2. Performance of the UBG for HDPEs with varying crystallinity

Fig. 3 shows the  $I(q)$  versus  $q$  for NIST molecular weight standards, (a) 1482, (b) 1484, and (d) 1483. The scattering curve for a moderately crystalline Equistar 6180 sample is also presented in (c). Additionally, the fit to a Metallocene sample, 399L60, is shown in Fig. S2 in the Supporting Information. The solid lines show the UBG, eq (8), for each curve. A local fit to the high- $q$  part of the curves with a power-law decay of  $-4$  slope was first performed and the Porod prefactor,  $B_1$ , was determined and fixed in the fits to reduce the number of free parameters by one. The remaining fit parameters listed in Table 3 are the packing factor,  $p$ , the correlation distance (long period),  $\xi$ , the radius of gyration for the lamellar thickness level (level 1,  $R_{g,1}$ ), the irregular periodicity parameter,  $\delta$ , which reflects finite stack size and long-range stacking period variability and the disorder constant,  $k_1$ , which reflects local-misorientation of lamellae and interfacial electron density gradients.

Using the fit parameters discussed previously in eq (4), the lamellar scattering pattern in the absence of correlations can be calculated.  $I_0(q)$  reflects the calculated scattering for the lamellae under dilute conditions and is used to determine the invariant for the system and, with the Porod prefactor, the  $S/V$  values in Table 4. The dilute scattering, dashed curves in Fig. 3(a)–(d), exhibits two power-law regimes (lines in the log-log plots). The low- $q$  power-law regime is the Lorentz region of the curve where a power-law of  $-P_2=-d_f=-2$  is observed, where  $d_f$  is the mass-fractal dimension of 2 for a lamella, here a disk. This region is terminated at low- $q$  by the Guinier regime for the overall disk although this regime is beyond the low  $q$ -range in Fig. 3(a)–(d). At the high- $q$  limit of the Lorentz region of  $q$  a second Guinier knee is observed for the thickness of the lamellae. This is followed by a Porod regime,  $q^{-4}$ , reflecting the smooth surface of the lamellae. This surface scattering region coincides with the uncorrelated calculation, eq (4), and the UBG, allowing for the independent determination of the power-law prefactor by a local fit prior to the UBG fit to account for lamellar correlations, eq (8).

### 3.3. Distortions and thickness of the lamellar structure in semi-crystalline polymers

In this study, several cases have been observed where the lamellar structure is distorted, reminiscent of the behavior previously observed for uncorrelated lamellar crystallites [6,42,43]. An example of attempts to use the UBG and the resulting fit is shown below, Fig. 4(a) for HDPE from a highly spherulitic sample (Equistar BS H) that displays strongly

**Table 3**

Fit parameters for the proposed UBG in eq (8) for the various polyethylene grades. Note that generally,  $B_1$  can be fixed through a high- $q$  Porod fit. (Errors are propagated from the counting errors.)

Polyethylene	$B_1(\times 10^{-8})$ ( $\text{\AA}^{-4}$ or $\text{cm}^{-1}\text{\AA}^{-4}$ ) <sup>d</sup>	$R_{g,1}$ ( $\text{\AA}$ )	$\xi$ ( $\text{\AA}$ )	$p$	$k_1$	$\delta$
NIST 1482 <sup>a</sup>	7.1 ( $\pm 0.07$ )	101 ( $\pm 1$ )	242 ( $\pm 1$ )	168 ( $\pm 3$ )	0.019 ( $\pm 0.001$ )	0.17 ( $\pm 0.01$ )
NIST 1483 <sup>a</sup>	8.8 ( $\pm 0.05$ )	135 ( $\pm 7$ )	287 ( $\pm 2$ )	199 ( $\pm 30$ )	0.044 ( $\pm 0.007$ )	0 ( $\pm 0.01$ )
NIST 1484 <sup>a</sup>	6.9 ( $\pm 0.04$ )	140 ( $\pm 3$ )	313 ( $\pm 1$ )	82 ( $\pm 5$ )	0.03 ( $\pm 0.002$ )	0 ( $\pm 0.01$ )
Equistar 6180 <sup>a</sup>	9.3 ( $\pm 0.07$ )	109 ( $\pm 1$ )	284 ( $\pm 1$ )	93 ( $\pm 2$ )	0.018 ( $\pm 0.001$ )	0 ( $\pm 0.01$ )
Equistar BS A <sup>b</sup>	1180 ( $\pm 4$ )	99 ( $\pm 3$ )	199 ( $\pm 1$ )	89 ( $\pm 9$ )	0.044 ( $\pm 0.005$ )	0 ( $\pm 0.01$ )
Equistar BS H <sup>b</sup>	1245 ( $\pm 5$ )	93 ( $\pm 1$ )	200 ( $\pm 1$ )	57 ( $\pm 2$ )	0.034 ( $\pm 0.001$ )	0.07 ( $\pm 0.01$ )
Metallocene 399L60 <sup>c</sup>	1460 ( $\pm 8$ )	57 ( $\pm 0.5$ )	176 ( $\pm 1$ )	49 ( $\pm 1$ )	0.039 ( $\pm 0.0003$ )	0 ( $\pm 0.01$ )

<sup>a</sup>refer Fig. 3 for the fit. <sup>b</sup>refer Fig. 4 for the fit. <sup>c</sup>refer Fig. S2 in the Supporting Information for the fit. <sup>d</sup>units of  $\text{cm}^{-1}\text{\AA}^{-4}$  for absolute intensity measurements (b,c) and  $\text{\AA}^{-4}$  for relative intensity measurements (a).

fibrillar colloidal structure. A similar sample (Equistar BS A), Fig. 4(b), that does not display strong spherulitic structure, contains broader colloidal scale lamellae, and is more laterally symmetric is also shown. The two samples display identical bulk degrees of crystallinity,  $\phi_{\text{DSC}}$  (Table 1), but differ in the long-chain branch content as measured through rheology [52–54]. Equistar BS A has a much higher long-chain branch content than Equistar BS H, as mentioned in the experimental section. One manifestation of this is the strong spherulitic structure displayed by Equistar BS H on the micron scale ( $q < 0.001 \text{\AA}^{-1}$ ) associated with strong fibrillar growth habits on the colloidal-to nano-scale ( $0.001 \text{\AA}^{-1} < q < 0.01 \text{\AA}^{-1}$ ) [55–57]. Equistar BS A displays a highly lamellar, 2-d growth habit on the nano-scale that is associated with poorly organized spherulitic structures in this sample. The two samples display similar lamellar thicknesses but different aspect ratios in Table 4.

The scattering data in Fig. 4(a) and (b) are fit to the intermediate- $q$  regime as indicated by the dashed vertical lines. This fit is extrapolated to low- $q$  for a comparison of the fit prediction in the lamellar scaling regime based on the laterally symmetric lamellar model used in this paper. For Equistar BS H in Fig. 4(a) the agreement for the fit projection is rather poor in this region since the lamellar stacks are highly fibrillar. This high degree of asymmetry is associated with good spherulitic structure at lower- $q$  ( $q < 0.001 \text{\AA}^{-1}$ ) [55–57]. For weakly spherulitic Equistar BS A, the extrapolated agreement in this regime is much better, Fig. 4(b). The bulk crystallinity of Equistar BS A from Table 1 is 0.68 which reflects both the amorphous between lamellae within stacks, as well as the amorphous separating lamellar stacks. This differs from the local crystallinity from SAXS, that is about 0.99. The local crystallinity value may be artificially high due to polydispersity in lamellar thickness since it is obtained from  $\phi = t/\xi$  and  $t = 2R_{g,1}$ . The radius of gyration is obtained from the square root of the eight to the sixth moments of size,  $R_g^2 \sim \langle R^8 \rangle / \langle R^6 \rangle$  [48]. For a polydisperse distribution of size,  $R_g$  will reflect the largest representatives of the population (the boulders on a sandy beach). We can estimate the polydispersity in thickness through the polydispersity index for thickness,  $PDI = B_1 R_{g,1}^4 / G_1$ , for disks of large aspect ratio where disks with monodisperse thickness have a value of  $PDI = 1$  [61]. For the polyethylene samples in this study  $PDI$  varies within a narrow range from 1.2 to 1.4 indicating moderate polydispersity in lamellar thickness.

High values of the local degree of crystallinity could occur if domains of crystals form in samples such as block copolymer polyolefins, as discussed below. In these cases, most of the amorphous material lies between the lamellar stacks while the crystallinity is quite high within the stacks. Quantification of this distinction has not previously been strongly made in the literature. One advantage of the UBG is that the extent of the two types of amorphous can be quantified if the bulk crystallinity is measured using XRD, calorimetry or density. The stack/local degree of crystallinity is determined from the ratio of the lamellar thickness, obtained from the radius of gyration, and the correlation distance determined from the position of the correlation peak. Auriemma et al. [60] also report the local crystallinity from the peak features in the autocorrelation and interface distribution functions which was about 3–4 times larger than the bulk crystallinity from WAXS or DSC. The two values reflect different moments,  $R_g$  reflecting the square root of the eight to the sixth moment (for instance as described by Roe [48]), while the correlation distance reflects a lower order moment, obtained from a Gaussian fit to the second order moment. For polydisperse distances  $R_g$  will skew towards a larger value since it is a higher order moment while the correlation distance will skew towards the mean. Then the ratio could yield an overly large value of the local degree of crystallinity within a stack for polydisperse lamellar thicknesses.

In Figs. 3 and 4, it can be observed that for a high degree of crystallinity, the proposed UBG can easily resolve the second order scattering peak especially when the second order peak falls close to  $2q^*$ , twice the position of the first order peak,  $q^*$ . As disorder increases the second order peak becomes weaker and the second order peak position

**Table 4**

Average lamellar morphological features derived from the fit parameters in Table 3.  $t$  is  $2R_{g,1}$ ;  $t_z$  is from  $S/V$  and the invariant;  $t_L$  is from  $\phi_{DSC}$  and the long period.  $\Delta\phi$  is the difference between SAXS and DSC values for the degree of crystallinity whereas,  $\phi_{a(NS)}$  is the fraction non-stack amorphous. (Errors are propagated from the counting errors.)

Polyethylene	$\phi_{SAXS}$ or $\phi$	$\Delta\phi$	$\phi_{a(NS)}$	$S/V$ (m <sup>2</sup> /cm <sup>3</sup> )	$t$ (Å)	$t_z$ (Å)	$t_L$ (Å)	$R$ (Å)	A, Aspect Ratio
NIST 1482	0.84 (±0.002)	-0.01	-0.11	54 (±1)	202 (±2)	310	224	1010 (±10)	10 (±0.1)
NIST 1483	0.94 (±0.005)	0.18	0.13	51 (±1)	270 (±14)	368	236	1390 (±110)	10 (±1)
NIST 1484	0.90 (±0.002)	0.30	0.26	51 (±1)	281 (±6)	351	208	950 (±30)	6.8 (±0.2)
Equistar 6180	0.77 (±0.001)	0.04	-0.02	65 (±1)	218 (±2)	236	222	850 (±10)	7.8 (±0.1)
Equistar BS A	0.99 (±0.005)	0.32	0.23	78 (±2)	198 (±6)	256	153	660 (±40)	6.7 (±0.4)
Equistar BS H	0.93 (±0.002)	0.26	0.19	75 (±1)	186 (±2)	247	151	510 (±10)	5.5 (±0.1)
Metallocene 399L60	0.65 (±0.001)	0.30	0.54	129 (±2)	114 (±1)	100	53	350 (±3)	6.2 (±0.05)

**Table 5**

Fit parameters for the proposed UBG function in eq (8) for other semi-crystalline polymers from literature. Additional fit parameters per the modified correlated fit in eq (9) to account for the domains in the block copolymer samples are also listed.

Polymer	$B_1$ (Å <sup>-4</sup> )	$R_{g,1}$ (Å)	$\xi$ (Å)	$p$	$k_1$	$\delta$
Starch in aqueous gel [19]	$1.6 \times 10^{-7}$	39.7	88.5	13.7	0.027	0.68
Starch in aqueous gel [58]	$4.3 \times 10^{-7}$	38.7	87.1	47.7	0.016	0.45
LDPE - 250 kg/mol [59]	$4.4 \times 10^{-8}$	38.6	170	19	0.045	0.004
EOBC-115 kg/mol [60] <sup>1</sup>	$1.04 \times 10^{-1}$	26.7	82.5	4.6	0.017	0.0012
EOBC-130 kg/mol [60] <sup>3</sup>	$2.15 \times 10^{-1}$	30.5	88.3	4.0	0.011	0.0005

Additional fit parameters to account the larger domain structural level, eq 9				
Polymer	$G_3$	$R_{g,3}$ (Å)	$B_3$ (Å <sup>-4</sup> )	$R_{g,cut-off}$ (Å)
EOBC-115 kg/mol [60]		$5.6 \times 10^6$	135.9	0.17
EOBC-130 kg/mol [60]		$1.3 \times 10^5$	135.6	0.004

moves to  $q > 2q^*$ . The UBG model can accommodate this to a certain extent with the disorder parameters, however, there is some limitation to this accommodation. In the case where the second order peak is much larger than  $2q^*$  the fit ignores the second order peak. Although, this is a limitation of the function, it seems that useful information can still be obtained from the fit. A wide range of possible scattering patterns are

shown in Figs. 3 and 4 and S2 in the Supporting Information, so that not only the best fits are shown.

Three different measurements of the lamellar thickness,  $t$ ,  $t_z$ , and  $t_L$ , were determined from the UBG model. The structural model directly yields the lamellar thickness,  $t=2R_{g,1}$ . The z-average thickness,  $t_z$ , was calculated using  $t_z=20000\phi(S/V)^{-1}$  (from equation 3, p. 216 in Ref. [62]), with  $t_z$  in Ångström,  $S/V$  in m<sup>2</sup>/cm<sup>3</sup>, and  $\phi=t/\xi$  with  $t=2R_{g,1}$ .  $S/V$  can be obtained through normalization of  $B_1$  by the Porod invariant,  $Q = \int_0^\infty I_0(q)q^2 dq$ , and through numerical integration based on the fit parameters in Table 3 for the uncorrelated scattering function,  $I_0(q)$ , in eq (4) such that,  $S/V=\pi B_1/Q$ . The thickness from Lorentz corrected data,  $t_L=\phi_{DSC}\xi_L$  was also determined. Fig. 5 compares these three results for lamellar thickness. The general trend is that the  $S/V$  thickness,  $t_z$ , is larger than the direct fit and the difference is larger for thicker crystals. This means that the  $S/V$  ratio is smaller than expected from the fitted lamellar thickness for thicker lamellae. In obtaining the thickness from  $S/V$  we are assuming that  $S/V \sim 2/t$ , that is, there is no contribution to the specific surface area from the lateral sides of the lamellae, i.e., the aspect ratio is  $\infty$ . For a lamellar disk with a finite aspect ratio  $S/V \sim 2/t + 2/R = 2/t(1 + 2/A)$ . This correction largely brings agreement between  $t$  and  $t_z$ , Fig. 5.

The difference between  $t$  from UBG and  $t_L$  is partly due to the difference between the local degree of crystallinity within a stack of lamellae,  $\phi_{SAXS}=t/\xi$ , and the degree of crystallinity measured by DSC,  $\phi_{DSC}=t_L/\xi_L$ .  $\phi_{DSC}$  should be smaller since it includes non-local amorphous such as interfibrillar or interspherulitic amorphous material. This would result in a smaller value for  $t_L$  compared to  $t$  from the fit. Another complication is that  $t$  includes perfect crystalline regions and regions of

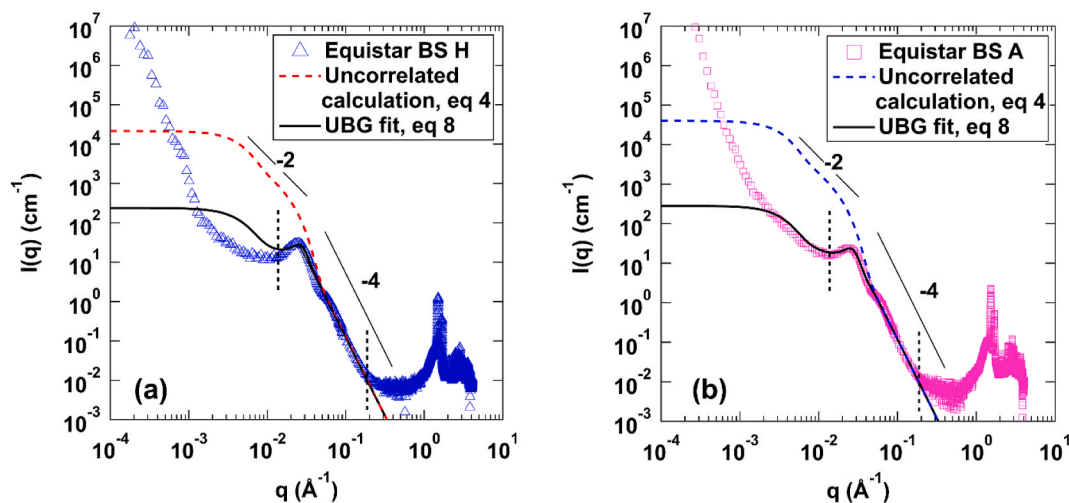


**Fig. 4.**  $I(q)$  versus  $q$  for two polyethylene samples. The fit range is  $0.012 \text{ \AA}^{-1} < q < 0.16 \text{ \AA}^{-1}$  as indicated by the dashed vertical lines for both plots. The fit has been extrapolated to a wider  $q$ -range for comparison as discussed in the text. The dashed curves represent the fits in the absence of correlations, eq (4). (a) SAXS and extrapolated high- $q$  UBG (eq (8)) for highly spherulitic long chain branching standard, Equistar BS H; and (b) for weakly spherulitic long chain branching standard, Equistar BS A.

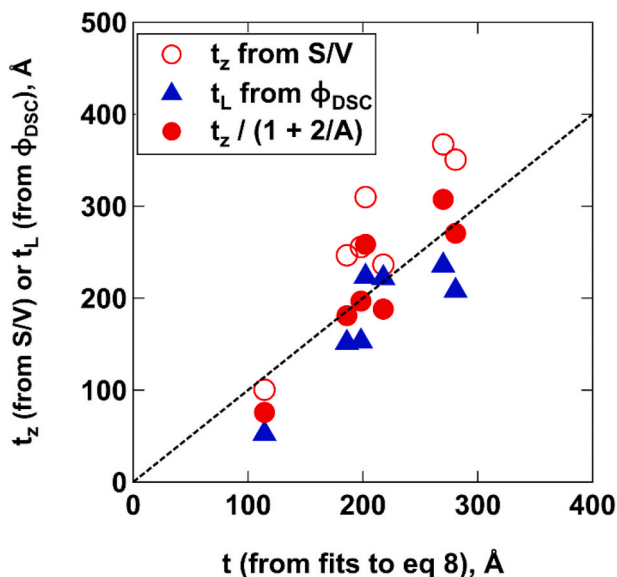


Fig. 5. Comparison of the z-average thickness,  $t_z$ , and the thickness from the Lorentz corrected data,  $t_L$ , with the thickness obtained from fits to the SAXS data,  $t$ , per the proposed model in eq (8).  $t_z$  normalized by  $(1+2/A)$ , where  $A$  is the aspect ratio, agrees with  $t$ .

high electron density at the interface of the lamellae. It is possible that  $t_L$  could be larger than  $t$  in some cases where a significant lamellar surface density gradient exists. This seems not to be the case since  $t$  is generally larger than  $t_L$ , except for one sample, NIST 1482 (Fig. 3(a)). The fraction of the sample that is due to amorphous not in lamellar stacks is given by  $\phi_{a(NS)} = t_L(\{1/t_L\} - \{1/t\})$ . This relationship can be obtained by considering,  $t_L = \xi_L(M_c / \{M_c + M_{a(T)}\})$  and  $t = \xi(V_c / \{V_c + V_{a(S)}\}) = \xi(M_c / \{M_c + M_{a(S)}(\rho_c/\rho_a)\})$ , where  $M_c$ ,  $M_{a(T)}$ ,  $M_{a(S)}$ ,  $V_c$ ,  $V_{a(T)}$ , and  $V_{a(S)}$  represent the weight and the volume of crystallites, the total amorphous and the local amorphous within the lamellar stacks, respectively. The amorphous weight fraction that is not within the stacks is thus,  $\phi_{a(NS)} = (W_{a(T)} - W_{a(S)}) / (W_c + W_{a(T)}) \approx t_L(\{1/t_L\} - \{1/t\})$ , assuming  $\xi \approx \xi_L$  from Fig. 6 and  $\rho_c/\rho_a \approx 1$ . In reality,  $\rho_c$  is  $\sim 1 \text{ g/cm}^3$  and  $\rho_a$  is  $\sim 0.85 \text{ g/cm}^3$  for polyethylene. Thus, the actual amorphous weight fraction not within the stacks is slightly larger than the reported values of  $\phi_{a(NS)}$ . For some samples, Metallocene 399L60 (Fig. S2 in the Supporting Information), more than half of the sample's amorphous polymer is non-stack amorphous. Generally, samples with a smaller fraction of amorphous within the stack would result in a larger packing factor,  $p$ .

### 3.4. Lamellae: local crystallinity within stack, aspect ratio, orientation, and alignment

Table 4 shows the average morphological parameters for the lamellae derived from the fit results in Table 3. Significant clustering of the lamellar stacks, as measured by the discrepancy between  $\phi$  ( $\phi_{SAXS}$  in Table 4) and  $\phi_{DSC}$  in Table 1, was observed. For the NIST 1482 sample in Fig. 3(a), the local crystallinity from SAXS ( $\phi = t/\xi = R_{g,1}/\xi$ ) of 0.84 from Table 4, is approximately equal to the bulk crystallinity,  $\phi_{DSC}$  in Table 1. For NIST 1484 in Fig. 3(b),  $\phi_{DSC}$  is 0.60 in Table 1 deviates considerably from  $\phi$  of 0.89 from Table 4. This sample displays somewhat thicker lamellae compared with the other isothermally crystallized molecular weight standard samples. A larger discrepancy between bulk ( $\phi_{DSC}$ ) and local crystallinity ( $\phi$ ) indicates a large extent of segregation of lamellar stacks, i.e., higher amount of interfibrillar or interspherulitic amorphous regions. Similarly, NIST 1483 in Fig. 3(d) displays a significantly enhanced local crystallinity from SAXS,  $\phi = 0.94$ , compared to  $\phi_{DSC}$  which indicates a higher extent of segregation of lamellar clusters as compared to Equistar 6180 which has the same overall bulk crystallinity

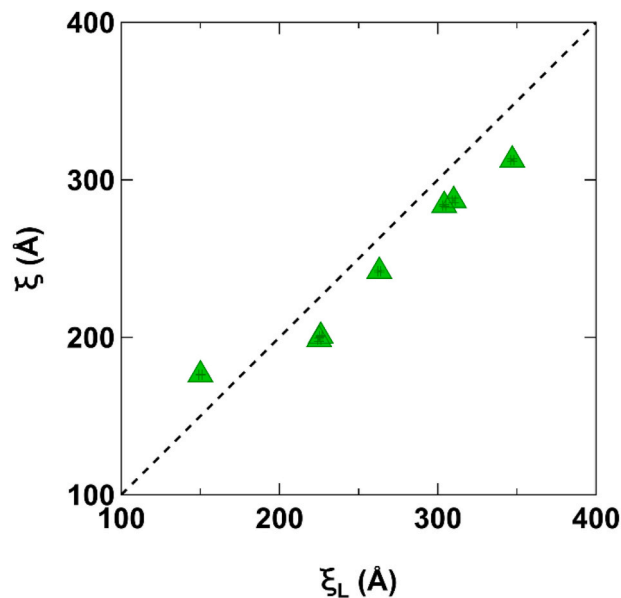


Fig. 6. Comparison of the long period (1-d correlation length),  $\xi$ , from fits per eq (8) by directly fitting the scattering intensity,  $I(q)$ , with the long period,  $\xi_L$ , from a Gaussian fit to the Lorentz corrected data,  $I(q)q^2$  versus  $q$ . Discrepancies between the two values may be due to the inaccuracy in the assumption of the Lorentz correction that the data follows a power-law of  $-2$  in the regime of the correlation peak.

from Table 1, but a considerably different local crystallinity. Consequently, Equistar 6180 shows only a small extent of clustering of lamellar stacks. Although,  $\phi_{DSC}$  represents the weight fraction crystallinity, whereas  $\phi$  indicates the volume fraction crystallinity, even after accounting for the relative densities of the crystalline and amorphous phases for HDPE,  $\phi$  is expected to be larger than  $\phi_{DSC}$ . This is because  $\phi$  is a measure of the local crystalline fraction within a lamellar stack,  $\phi$ , whereas  $\phi_{DSC}$  is a bulk measurement.  $\phi_{DSC}$  should have a lower value since it includes the amorphous which is not between the stacked lamellae,  $\phi_{a(NS)}$ . This is important information since it quantifies the segregation of lamellar stacks.

The correlation distances (long periods),  $\xi$ , from the fits listed in Table 3, are slightly less than the long periods determined from a Gaussian fit to the Lorentz corrected data,  $\xi_L$  in Fig. 6. The Lorentz fit value,  $\xi_L$ , was used as an initial value in the least-squares minimization of the fits. Additionally, an initial estimate for minimization of  $R_{g,1}$  was obtained from  $R_{g,1} = \xi_L \phi_{DSC} / 2$ . This slight deviation between  $\xi_L$  and  $\xi$  can be reconciled when considering the extent of the power-law  $-2$  slope in the uncorrelated lamellar curves in Figs. 3 and 4. The assumption of the Lorentz correction is that the correlation peak is embedded in the power-law  $-2$  regime, which appears as a line of slope  $-2$  in a log-log plot. However, in Figs. 3 and 4 the power-law regime at low- $q$  for the calculated uncorrelated lamellae, dashed line, does not extend to the  $q$  range of the peak, so multiplying the intensity by  $q^2$  in the Lorentz correction will erroneously shift the correlation peak to the left in  $q$ , that is to larger sizes, since the data actually has a steeper slope in the peak regime due to the influence of the Guinier regime on the power-law regime. This influence of the Guinier regime on the power-law regime is correctly accounted for in the UBG model leading to the correct and smaller correlation length in the Unified fits. For the Metallocene resin (Fig. S2 in the Supporting Information) that shows the smallest long period in Fig. 6, the correlation peak does occur within but at the edge of the  $-2$  power-law regime. Due to the low crystallinity, the Guinier regime is more prominent in the scattering curve. This leads to an artificially broadened peak in the scattering data towards higher- $q$ , shifting the Lorentz corrected peak to the right, resulting in an erroneously lower Lorentz correlation length for that sample. By inspection of

the uncorrelated lamellar curves, it becomes evident that the Lorentz correction can introduce errors in the estimated correlation distance.

The polyethylene samples analyzed in this study have variable thermal histories and molecular-weight polydispersity since some are model polymers and some commercial samples. Nonetheless, the lamellar aspect ratio,  $A=D/t=2R/t$ , decreases linearly with the weight average molecular weight, Fig. 7(a), with the more polydisperse samples generally showing a slightly lower aspect ratio. The average lamellar radius/lateral extent,  $R$ , in Table 4 was calculated using eq (6),  $R=\sqrt{\{(pR_{g,1}\xi)/4\}}$ . The lamellar thickness is generally controlled by the crystallization temperature through the Hoffman-Lauritzen expression. The thermal history is not a control parameter through the studied samples, though the NIST samples and Equistar 6180 were approximately isothermally crystallized at 120 °C (crystallization is quite rapid in polyethylene and the SAXS samples have significant thickness hindering efforts towards a step-jump thermal quench).

It is interesting to speculate on how the molecular weight could impact the aspect ratio, outside of viscosity and the diffusion coefficient which are strongly dependent on temperature and apparently do not play an obvious role. The contour length of the chains,  $L$ , can be estimated by the number of monomers in the chain and about 2.55 Å repeat distance per monomer (for the c-axis unit cell parameter in a planar zig-zag conformation). For the shortest chains, NIST 1482, of 13.6 kg/mol, the contour length (path length of the blue line in Fig. 8), is about 1,250 Å while for the largest chains, BS H, of about 150 kg/mol,  $L\sim 14,000$  Å. Dividing by the thickness of the lamellae, the shortest chain has the possibility of about 6 chain folds per chain while the longest chain (BS H) has the possibility of about 66 chain folds per chain. The “b” lattice spacing is 4.94 Å so the shortest chain could span a lateral size of only 29 Å in the lamella, while the longest chain could span a lateral size of 326 Å.  $2R$  for NIST 1482 is about 2,100 Å whereas, it is about 970 Å for Equistar BS H, Table 4. So, the low molecular weight chains require at least 72 chains to reach from one side of the lamella to the other side, while for the high molecular weight a minimum of 3 chains can reach a lamellar diameter in the crystallite. The two lowest HDPE points in Fig. 7 (a) (red) to the right are for the long-chain branched Equistar BS H and BS A samples. At high molecular weights we expect more chain entanglements per chain. It seems plausible that topological constraints such as long-chain branching, and chain entanglements have a direct link to the lateral growth of lamellae and to the lamellar aspect ratio.

The topology of the chains including the number of entanglements

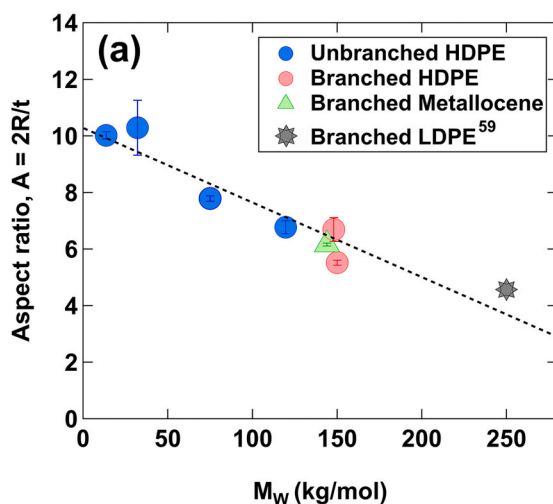


Fig. 7. (a) The aspect ratio of lamellae derived from the fitting result (Table 4) as a function of the weight average molecular weight of the polymer (Table 1) and a commercial LDPE sample from Ref. [59] discussed below; (b) A schematic showing the reduction in aspect ratio for higher molecular weight specimens due to branch points in the chain that serve as topological constraints.

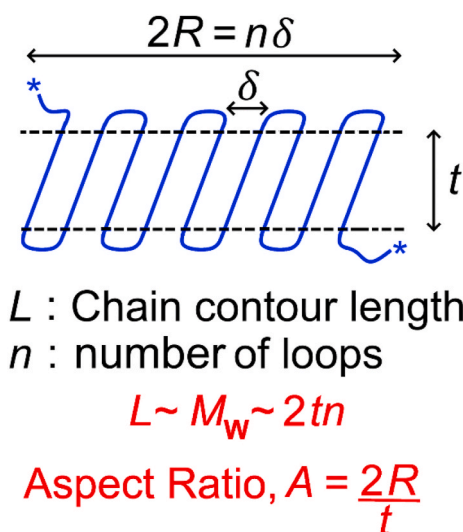
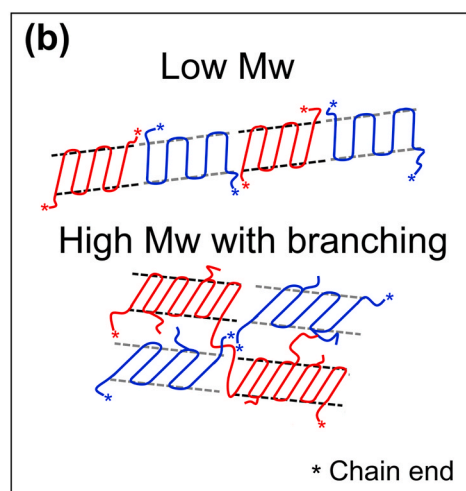
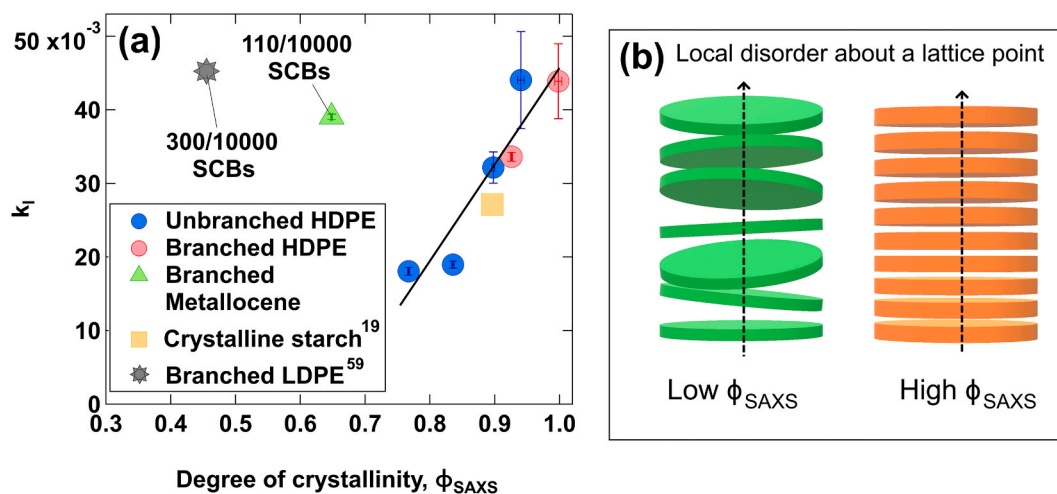


Fig. 8. How a polymer chain fits into a lamella.

and branch sites impact the aspect ratio. The entanglement molecular weight for polyethylene is around 1600 g/mol. The lowest molecular weight chains in this study have about 9 entanglements while the highest molecular weight have about 90 per chain. For a branched chain with 1 branch per 1000 carbons (13.6 kg/mol for example) there are about 11 branch points in an average chain. Branch points are much stronger topological constraints compared to entanglements. Although a quantitative model has not been reached concerning the observed apparent linear dependence of aspect ratio on the weight average molecular weight, Fig. 7(a), the high extent of entanglements per chain, and the presence of long-chain branching, may lead to crystals with many more dangling ends which might disrupt the lateral extent,  $2R$ , for the lamellae as shown schematically in Fig. 7(b).

Fig. 9(a) shows that the Debye-Waller disorder parameter,  $k_1$ , increases linearly with the degree of crystallinity except for the Metallocene polymer 399L60.  $k_1$  is effectively the inverse of the variance,  $k_1 \sim 1/2\sigma^2$ , for a Gaussian distribution of electron density about the lattice point. An increase in  $k_1$  with the degree of crystallinity in a stack indicates that the lamellae are more tightly bound to their lattice





**Fig. 9.** (a) Dependence of the local lamellar orientation,  $k_l$  as a function of the local degree of crystallinity,  $\phi_{\text{SAXS}}$ , for branched HDPE (Equistar BS A, BS H indicated by red circles), unbranched HDPE (NIST 1482, 1483, 1484 and Equistar 6180 indicated by blue circles), low density Metallocene 399L60 (green triangle); crystalline starch in aqueous gel [19] (yellow square) and branched LDPE [59] (grey star) discussed below; (b) Schematic of decreasing misalignment or improving lamellar orientation with increase in  $\phi_{\text{SAXS}}$  since  $k_l \sim 1/2\sigma^2$ . (For interpretation of the references to color in this figure legend, the reader is referred to the Web version of this article.)

positions as the local degree of crystallinity increases. Similarly, larger  $k_l$  indicates that there is less orientational disorder and lower interfacial broadening of the lamellae with a higher degree of local crystallinity as shown schematically in Fig. 9(b).

### 3.5. Extending the proposed UBG to other systems

The efficacy of the proposed model is tested on the scattering data for crystalline starch lamellae in an aqueous gel [19,58], commercial LDPE [59], and ether insoluble fractions of ethylene/1-octene block copolymers (EOBCs) [60].

#### 3.5.1. Starch lamellae in an aqueous gel

Cameron and Donald [19,63] proposed a direct fitting function to the SAXS data for aqueous gels of starch which was modeled by stacks

comprised of infinite, alternating crystalline and amorphous layers. Their function for stacked lamellae had six fitting parameters after appropriate background subtraction was performed: the amount of crystalline fraction,  $\phi$ ; the average repeat length in the stack or the correlation length,  $d$ ; the width of the thickness distribution,  $\beta$ ; the number of crystalline and amorphous pairs within a lamellar stack,  $N$ ; the electron density difference between the crystalline and amorphous layers within a stack,  $\Delta\rho$ ; and the electron density difference between the lamellar stack and the background,  $\Delta\rho_{\text{li}}$ . Fig. 10(a) shows an  $I(q)$  vs  $q$  plot (digitized from Figure 7(a), p. 2632 in Ref. [19]) whereas Fig. 10(b) shows the simulation result of an  $I(q)$  vs  $q$  plot (digitized from Figure 3, p. 317 in Ref. [58]) for different crystalline starch lamellae in aqueous gels. These curves were fit to the UBG from eq (8), and the fit results are reported in Table 5. Note that a background intensity of about 0.0012 in Fig. 10(a) was used to get a good fit in the high- $q$  Porod region.

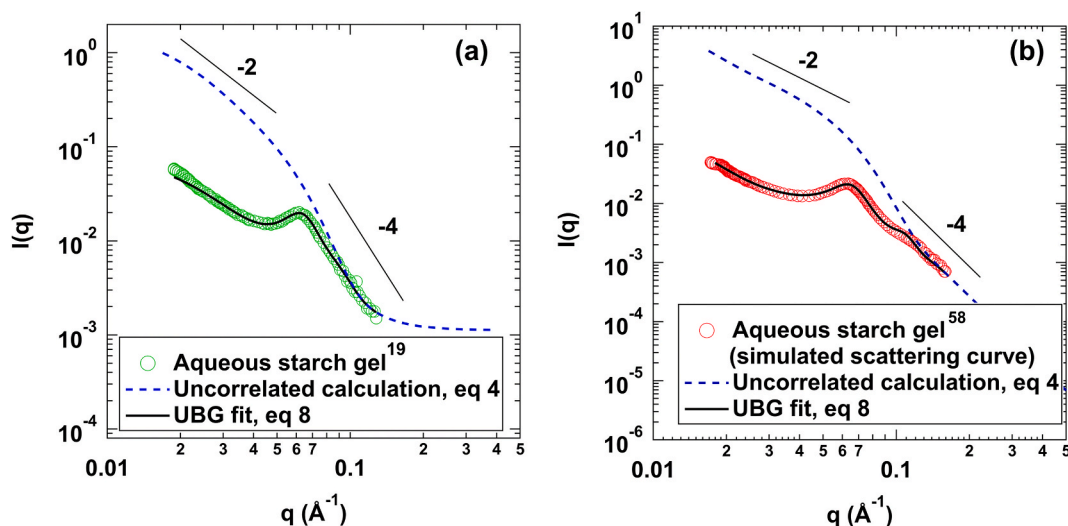


**Fig. 10.** (a) SAXS data on crystalline lamellae in a 45% aqueous starch slurry digitized from Ref. [19]. Note that for the UBG the fit range was  $0.025 \text{\AA}^{-1} < q < 0.13 \text{\AA}^{-1}$  in (a). This fit was extrapolated to a wider  $q$  range. (b) Simulated SAXS curve for crystalline lamellae in a 50% aqueous starch slurry digitized from Ref. [58]. The solid black lines indicate the UBG in eq (8) whereas the dashed line indicates the fit, eq (4), in the absence of correlations for both curves.

In Fig. 10(a), the long period from the proposed fit,  $\xi = 88.5 \text{ \AA}$  agrees with the reported repeat length of the stack,  $88.5 \text{ \AA}$ . However, the lamellar thickness,  $t = R_{g,1} \sim 79 \text{ \AA}$  is greater than the reported thickness of the starch crystallites,  $66 \text{ \AA}$  [19], which could be attributed to the deviation of the experimental SAXS curve and the fit around the peak in Ref. [19]. Similarly, in Fig. 10(b), the long period from the proposed fit,  $\xi = 87 \text{ \AA}$ , agrees with the reported repeat length of the stack,  $91 \text{ \AA}$  [58], whereas the lamellar thickness from UBG,  $t = R_{g,1} \sim 77 \text{ \AA}$ , is slightly larger than the reported thickness of the starch crystallites of  $70 \text{ \AA}$  [58]. Since the local degree of crystallinity,  $\phi = t/\xi = R_{g,1}/\xi$  is directly related to the lamellar thickness, the estimate from the UBG, eq (8), are about 20% and 15% greater than the reported values of 0.75 [19] and 0.77 [58]. An aspect ratio of about 2.8 is seen for the crystalline starch in Fig. 10(a) whereas the lateral size is about 5.2 times the thickness for the starch in Fig. 10(b). The local-misorientation,  $k_l$ , determined from the fit in Fig. 10(a), surprisingly follows the same trend with local crystallinity as the HDPE samples in Fig. 9(a) (green square). For both samples, the stacking is irregular as reflected by the large value of  $\delta$

### 3.5.2. Commercial LDPE with short-chain branching

Fig. 11 shows  $\log I(q)$  vs  $\log q$  (digitized from Figure 10, p. 34717 in Ref. [59]) for a commercial LDPE of  $M_w \sim 250 \text{ kg/mol}$  with extensive short chain branching (300 SCBs per 10,000 carbons in the chain). This curve was fit to the structural model proposed in eq (8) and the fit results are listed in Table 5. To get a good fit in the high- $q$  Porod region, a background intensity of about 0.002 was used.

For this high MW LDPE sample, the aspect ratio,  $A = 2R/t = \sqrt{(pR_{g,1}\xi)/4} = 4.57$  in agreement with the general trend observed for polydisperse PE samples in Fig. 7(a) (black star). Additionally, the large value of  $k_l$  at a low degree of crystallinity,  $\phi = t/\xi = R_{g,1}/\xi = 0.46$ , shows a similar behavior to the Metallocene 399L60 sample that has a high short-chain branch content in Fig. 9(a) (black star). The local crystallinity within a stack,  $\phi_{\text{SAXS}} \sim 0.46$  is larger than the reported bulk crystallinity from DSC measurements in Ref. [59],  $\phi_{\text{DSC}} \sim 0.37$ , as expected. Additionally, the correlation length estimated from the fit,  $\xi = 170 \text{ \AA}$  is on the same order as the reported [59] long period for this sample  $\sim 200 \text{ \AA}$ .

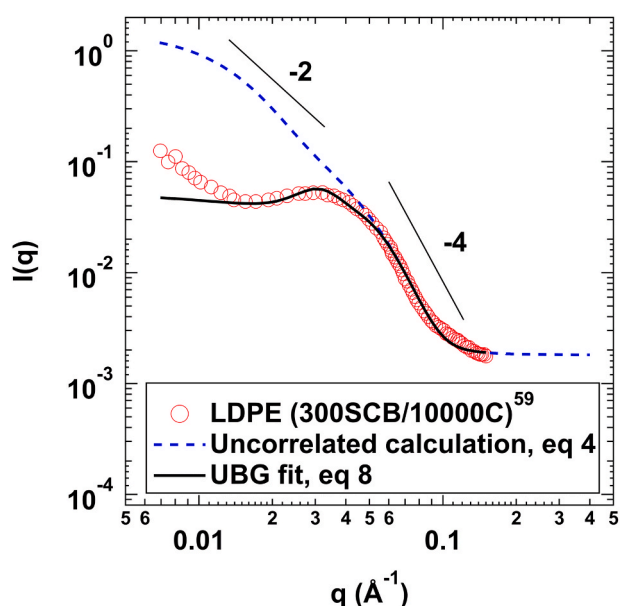


Fig. 11. SAXS data on commercial LDPE showing a correlated lamellae peak in scattering digitized from Ref. [59]. The solid black line indicates the UBG in eq (8) whereas the dashed line indicates the fit, eq (4), in the absence of correlations. Note that for the UBG,  $0.015 \text{ \AA}^{-1} < q < 0.1 \text{ \AA}^{-1}$ . This fit was extrapolated to a wider  $q$  range.

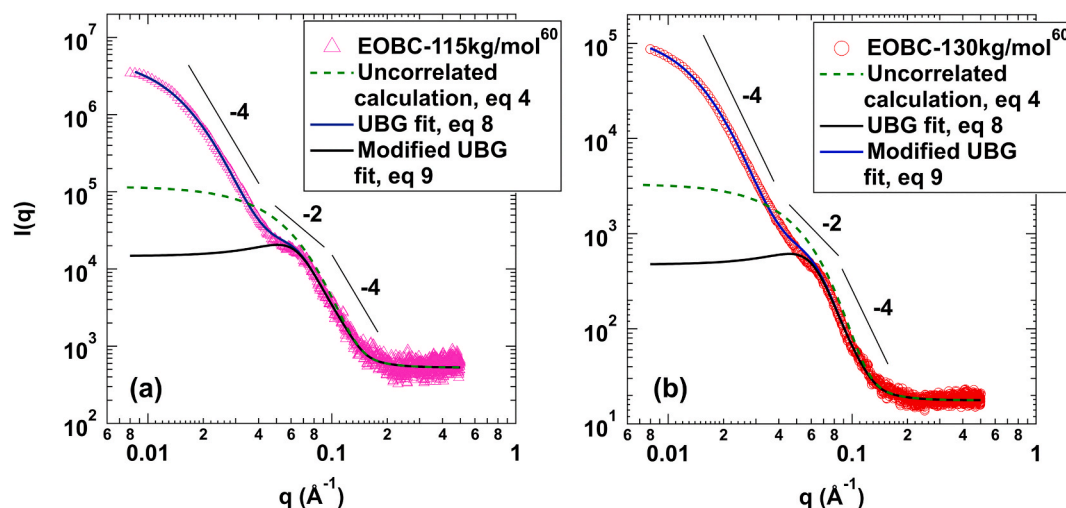
### 3.5.3. Commercial ethylene/1-octene block copolymers (EOBC)

Fig. 12 shows the  $I(q)$  vs  $q$  data from Figure 4A, p. 9620 in Ref. [60] for diethyl ether insoluble fractions of commercial thermoplastic elastomers (EOBCs) of two different molecular weights (115 kg/mol and 130 kg/mol). These samples are like Metallocene materials but with a higher melting point. Both samples were isothermally crystallized at  $110 \text{ }^\circ\text{C}$  as reported [60]. SAXS data in Fig. 12(a) and (b) were fit to the structural model proposed in eq (8) and the fit results are listed in Table 5. Note that the background intensity for fitting the SAXS intensity for EOBC-115 was about 530, whereas it was about 18 for the EOBC-130 in Fig. 12.

The crystalline lamellae for the 115 kg/mol block copolymer display an extremely low aspect ratio,  $A = 2R/t \approx 1.9$  which is slightly larger than  $A \approx 1.7$  for the 130 kg/mol BCP indicating that the aspect ratio decreases with increasing molecular weight as shown in Fig. 7(a). Auriemma et al. [60] have estimated the long period and the crystallite/amorphous thickness within a stack via autocorrelation of the electron density fluctuations as well as the interface distribution functions (IDF). For both specimens fit in Fig. 12, black curves, a local degree of crystallinity,  $\phi$ , of about 0.62 was reported by the IDF method in Ref. [60]. From Table 5,  $\phi = R_{g,1}/\xi$  is  $\sim 0.65$  for the 115 kg/mol and  $\sim 0.69$  for the 130 kg/mol block copolymers, close to the reported local crystallinity but much higher than the reported bulk DSC crystallinity of 0.13 [60]. The correlation length,  $\xi$ , of  $\sim 83 \text{ \AA}$  and a lamellar thickness of  $\sim 53 \text{ \AA}$  approximately agree with the reported values of  $\sim 81 \text{ \AA}$  and  $\sim 51 \text{ \AA}$  for the long period and crystallite thickness determined via from the IDF for EOBC-115 sample in Ref. [60], respectively. Similarly,  $\xi$  of  $\sim 88 \text{ \AA}$  and a lamellar thickness of  $\sim 61 \text{ \AA}$  agree with the reported values of  $\sim 92 \text{ \AA}$  and  $\sim 57 \text{ \AA}$  for the long period and crystallite thickness determined via from the IDF for EOBC-130 sample in Ref. [60]. A larger deviation in the long period estimated from the autocorrelation function and the interfacial distribution function is associated with greater structural disorder and is independent of the crystallization conditions [64]. This deviation is larger for EOBC-115 isothermally crystallized at  $110 \text{ }^\circ\text{C}$  as opposed to EOBC-130 crystallized under the same conditions as reported in Table 2, p. 9618 in Ref. [60]. A larger disorder in long spacing for EOBC-115 indicates greater irregularity in stacking period which is reflected in the larger value of  $\delta$  in Table 5 as compared to EOBC-130.

In addition to the uncorrelated calculation from the fit (dashed green curves in Fig. 12), eq (4), the modified UBG (blue curves in Fig. 12), eq (9), was also applied to account for the larger structural level corresponding to domains comprised of the crystalline lamellae stacks in a matrix of the amorphous rubber. The fit parameters to account for the domains are also listed in Table 5 for both EOBC-115 and EOBC-130 samples.  $R_{g,\text{cut-off}}$  is marginally greater than  $R_{g,2}$  for both block copolymers and represents the size scale where the surface of the large-scale crystalline domains becomes rough.

The fits to the modified UBG, eq (9), shown in Fig. 12(a) and (b) are consistent with two-phase systems that have domains with an equivalent spherical diameter,  $D_{\text{domain}} = 2\sqrt{(5/3)}R_{g,3}$  of approximately  $350 \text{ \AA}$ . The crystalline domain fraction of the sample is determined from the ratio of the bulk to the local crystallinity,  $\phi_{\text{DSC}}/\phi_{\text{SAXS}}$ . This has a value of approximately 0.2 for the EOBC-115 sample which indicates that the matrix is the amorphous phase (80%) with crystalline domains (20%). The cutoff size scale for the domains comprising of these low aspect lamellae (Table 5) indicates where the Porod's law (smooth surfaces) fails due to jutting crystalline lamellae at the interface.  $R_{g,\text{cut-off}}$  is the surface roughness size for asperities that make the surface rough. Additionally, the ratio of the Guinier prefactors for the domain and lamellae level,  $(G_3/G_2)+1$ , is a measure of the total average number of 1-d lamellae stacks within a domain. The total average lamella within a domain is about 61 for 115 kg/mol BCP and about 53 for the 130 kg/mol block copolymer. A cartoon of the multi-level hierarchical organization for these block copolymers based on the SAXS data is presented in Fig. 13.



**Fig. 12.** SAXS data on isothermally crystallized (at 110 °C) ether insoluble fractions of commercial block copolymers with molecular weights of (a) 115 kg/mol and (b) 130 kg/mol from Ref. [60]. The solid black lines indicate the UBG in eq (8) whereas the dashed line indicates the fit, eq (4), in the absence of correlations. Note that for the UBG the fit range was  $0.05 \text{ \AA}^{-1} < q < 0.5 \text{ \AA}^{-1}$  for both curves. To account for the larger semi-crystalline domains another structural level was added per eq (9) and represented by the solid blue curves in both plots. (For interpretation of the references to color in this figure legend, the reader is referred to the Web version of this article.)

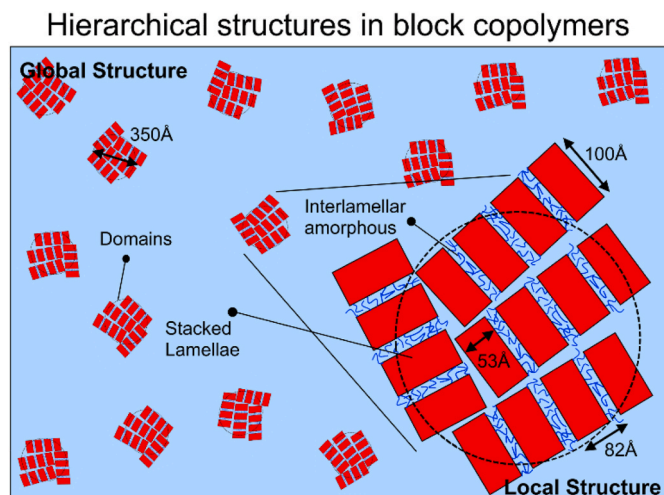


**Fig. 13.** Cartoon depicting the different hierarchical structures in isothermally crystallized block copolymer EOBC-115 from Ref. [60]. The domain size, long-period, lamellar thickness, and aspect ratio can be estimated from the proposed UBG fit model. Each 1-d stack comprises of approximately 65% crystalline lamellae. Note that although the spherical domains comprise of 61 lamellae, a 2-d projection would result in a lower number of crystalline lamellae in a domain of about  $61^{2/3} \sim 16$ .

#### 4. Conclusions

This paper describes direct fits of correlated lamellae in polyethylene samples using the Unified Function and a description of one-dimensional correlations based on the Born and Green approach. The UBG Function is sufficiently robust so that the same function can be used across a wide range of samples, and we have used this fit for HDPE, LDPE, LLDPE, Metallocene polyethylene as well as block copolymer, polyesters, and a crystalline starch gel. The UBG results in direct determination of the correlation distance ( $\xi$ ), lamellar thickness ( $t$ ), aspect ratio ( $A$ ), local degree of crystallinity within a stack of lamellae ( $\phi$ ), and the quality of the lamellar stacking in terms of packing density ( $p$ ), local disorder of

the Debye-Waller type ( $k_p$ ) and stacking disorder like Scherrer broadening ( $\delta$ ). For crystallites that are thought to have limited lamellar structure, such as highly spherulitic samples, deviations from the fit are evident at low- $q$ . These deviations could be accommodated in the proposed approach with additional parameters. A limitation of the proposed function is that the fit minimizes the deviation and ignores the second order peak at high- $q$  when the second order peak has a  $q$ -value much larger than  $2q^*$ .

Comparison is made with the Hermans (HF) and a hybrid Unified-Hermans function (HHF). The HF predicts a power-law of  $-2$  at low- $q$  which often disagrees with the data. There is ambiguity in the amorphous and crystalline sizes and the standard deviations and the meaning of two distinct standard deviations for the amorphous and crystalline phases in a stack seems confusing. Further, the calculated melting points from the HF and HHF functions do not agree with a Hoffman-Lauritzen analysis. The HHF can describe higher-level structures such as limits to the lamellar width and other higher order structures. Qualitatively, the UBG gives a better fit to the investigated data with smaller residuals.

The UBG based on the Unified Fit could serve to complement existing approaches to the analysis of SAXS data from semi-crystalline polymers such as long-period determination from the Lorentz corrected data and correlation function analysis. The UBG method offers several unique views on this complex structure such as measures of the non-stack amorphous, measures of the clustering of lamellae and the extent of stacking, the aspect ratio of lamellae, and a direct measure of the thickness that does not depend on a separate measure of the degree of crystallinity. The fit parameters correlate well with expectations and suggest new relationships that can be explored such as a linear dependence of the lamellar aspect ratio on the molar mass of the polymer. Since the Unified Function allows for calculation of the uncorrelated lamellar scattering curve, it makes possible an assessment of the appropriate range in  $q$  for application of the Lorentz dimensional correction. Separation of the structure and form factor in the Unified approach may allow for new understanding of the impact of thermal and mechanical history, chain structure, fillers, nucleating agents, and additives on the crystalline structure and the resulting physical properties.

## Notes

The authors declare no competing financial interest.

## CRediT authorship contribution statement

**Michael Camara:** Investigation, Writing – original draft, Writing – review & editing, Software, Validation, Formal analysis. **Kabir Rishi:** Investigation, Conceptualization, Data curation, Writing – original draft, Writing – review & editing, Software, Validation, Formal analysis, Visualization. **Gregory Beaucage:** Investigation, Conceptualization, Methodology, Software, Writing – original draft, Writing – review & editing, Supervision, Project administration. **Sathish K. Sukumaran:** Investigation, Writing – review & editing.

## Declaration of competing interest

The authors declare that they have no known competing financial interests or personal relationships that could have appeared to influence the work reported in this paper.

## Acknowledgements

This work was supported by the National Science Foundation through grant CMMI-1635865. Use of the Advanced Photon Source, APS, an Office of Science User Facility operated for the U.S. Department of Energy (DOE) Office of Science by Argonne National Laboratory, was supported by the U.S. DOE under contract no. DE-AC02-06CH11357. The USAXS data were collected at the APS on the beamline 9-ID-C operated by the X-ray Science Division. We would also like to thank Dr. Finizia Auriemma at the Department of Chemical Sciences at the University of Naples Federico II, Italy for providing the SAXS data for both ethylene/1-octene block copolymers in Ref. [60].

## Appendix A. Supplementary data

Supplementary data to this article can be found online at <https://doi.org/10.1016/j.polymer.2021.124281>. This includes all fitting codes used in the paper for the HF, HHF, and UBG functions.

## References

- [1] D.C. Bassett, *Principles of Polymer Morphology (Cambridge Solid State Science Series)*, Cambridge University Press, New York, US, 1981.
- [2] P.J. Phillips, Polymer crystals, *Rep. Prog. Phys.* 53 (1990) 549–604, <https://doi.org/10.1088/0034-4885/53/5/002>.
- [3] P.J. Phillips, Spherulitic crystallization in macromolecules, in: D.T.J. Hurl (Ed.), *Handb. Cryst. Growth. Vol. 2 Bulk Cryst. Growth. B Growth Mech. Dyn.*, Elsevier Science Publishers, New York, US, 1994, pp. 1168–1216.
- [4] J.J. Hermans, Über den Einfluss von Gitterstörungen auf das Röntgendiagramm, im Besonderen bei Gelen, *Recl. Des Trav. Chim. Des Pays-Bas.* 63 (1944) 211–218, <https://doi.org/10.1002/recl.19440631102>.
- [5] R. Hosemann, Röntgeninterferenzen an Strichgittern mit Flüssigkeitsunordnung, *Z. Phys.* 127 (1950) 16–40, <https://doi.org/10.1007/BF01338981>.
- [6] D. Pradhan, P. Ehrlich, Morphologies of microporous polyethylene and polypropylene crystallized from solution in supercritical propane, *J. Polym. Sci., Part B: Polym. Phys.* 33 (1995) 1053–1063, <https://doi.org/10.1002/polb.1995.090330709>.
- [7] R. Hosemann, Theorie der Röntgenstrahlenstreuung an partikelhaufen, *Z. Phys.* 113 (1939) 751–768, <https://doi.org/10.1007/BF01337604>.
- [8] D.J. Blundell, Models for small-angle X-ray scattering from highly dispersed lamellae, *Polymer* 19 (1978) 1258–1266, [https://doi.org/10.1016/0032-3861\(78\)90302-6](https://doi.org/10.1016/0032-3861(78)90302-6).
- [9] Norbert Stribeck, *X-Ray Scattering of Soft Matter*, Springer Berlin Heidelberg, Berlin, Heidelberg, 2007, <https://doi.org/10.1007/978-3-540-69856-2>.
- [10] F.J. Balta-Calleja, C.G. Vonk, *X-ray Scattering of Synthetic Polymers (Polymer Science Library, 8)*, Elsevier, New York, US, 1989.
- [11] G.R. Strobl, *The Physics of Polymers*, second ed., Springer Berlin Heidelberg, Berlin, Heidelberg, 1997 <https://doi.org/10.1007/978-3-662-03488-0>.
- [12] S. Kavesh, J.M. Schultz, Lamellar and interlamellar structure in melt-crystallized polyethylene. I. Degree of crystallinity, atomic positions, particle size, and lattice disorder of the first and second kinds, *J. Polym. Sci. 2 Polym. Phys.* 8 (1970) 243–276, <https://doi.org/10.1002/pol.1970.160080205>.
- [13] S. Kavesh, J.M. Schultz, Lamellar and interlamellar structure in melt-crystallized polyethylene. II. Lamellar spacing, interlamellar thickness, interlamellar density, and stacking disorder, *J. Polym. Sci. 2 Polym. Phys.* 9 (1971) 85–114.
- [14] W.E. Kaufman, J.M. Schultz, Lamellar and interlamellar structure in melt-crystallized polyethylene - Part 3 Effects of small deformation, *J. Mater. Sci.* 8 (1973) 41–46, <https://doi.org/10.1007/BF00755581>.
- [15] A. Bellare, H. Schnablegger, R.E. Cohen, A small-angle X-ray scattering study of high-density polyethylene and ultrahigh molecular weight polyethylene, *Macromolecules* 28 (1995) 7585–7588, <https://doi.org/10.1021/ma00127a001>.
- [16] S. Rabiej, M. Rabiej, K. Adamczyk-Tomiak, An intensity superposition model to fit the small angle X-ray scattering of semicrystalline polymers and its application to the monitoring of non-isothermal crystallization, *Eur. Polym. J.* 69 (2015) 247–259, <https://doi.org/10.1016/j.eurpolymj.2015.06.011>.
- [17] S. Fischer, Z. Jiang, Y. Men, Analysis of the lamellar structure of semicrystalline polymers by direct model fitting of SAXS patterns, *J. Phys. Chem. B* 115 (2011) 13803–13808, <https://doi.org/10.1021/jp204998p>.
- [18] Z.G. Wang, B.S. Hsiao, N. Sanjeeva Murthy, Comparison of intensity profile analysis and correlation function methods for studying the lamellar structures of semicrystalline polymers using small-angle x-ray scattering, *J. Appl. Crystallogr.* 33 (2000) 690–694, <https://doi.org/10.1107/S0021889899014193>.
- [19] R.E. Cameron, A.M. Donald, A small-angle X-ray scattering study of the annealing and gelatinization of starch, *Polymer* 33 (1992) 2628–2635, [https://doi.org/10.1016/0032-3861\(92\)91147-T](https://doi.org/10.1016/0032-3861(92)91147-T).
- [20] G.R. Strobl, N. Müller, Small-angle x-ray scattering experiments for investigating the validity of the two-phase model, *J. Polym. Sci. 2 Polym. Phys.* 11 (1973) 1219–1233, <https://doi.org/10.1002/pol.1973.180110613>.
- [21] R. Hosemann, A. Schönfeld, W. Wilke, Small angle scattering, in: *Adv. Struct. Res. By Diffr. Methods*, 3, Pergamon Press, New York, US, 1970, pp. 101–172, <https://doi.org/10.1016/B978-0-08-017543-0.50005-5>.
- [22] G. Kortleve, C.G. Vonk, X-ray small-angle scattering of bulk polyethylene - III. Results, *Kolloid-Z. Z. Polym.* 225 (1968) 124–131, <https://doi.org/10.1007/BF02086186>.
- [23] C.G. Vonk, G. Kortleve, X-ray small-angle scattering of bulk polyethylene - II. Analyses of the scattering curve, *Kolloid-Z. Z. Polym.* 220 (1967) 19–24, <https://doi.org/10.1007/BF02086052>.
- [24] L.E. Alexander, *X-ray Diffraction Methods in Polymer Science*, John Wiley & Sons, New York, US, 1969.
- [25] C. Marega, A. Marigo, G. Cingano, R. Zannetti, G. Paganetto, Small-angle X-ray scattering from high-density polyethylene: lamellar thickness distributions, *Polymer* 37 (1996) 5549–5557, [https://doi.org/10.1016/S0032-3861\(96\)80440-X](https://doi.org/10.1016/S0032-3861(96)80440-X).
- [26] B.S. Hsiao, Semicrystalline polymers: lamellar morphology by SAXS. *Encycl. Mater. Sci. Technol.*, Elsevier, 2002, pp. 1–6, <https://doi.org/10.1016/B0-08-043152-6/01807-6>.
- [27] C. Marega, A. Marigo, V. Causin, Small-angle X-ray scattering from polyethylene: distorted lamellar structures, *J. Appl. Polym. Sci.* 90 (2003) 2400–2407, <https://doi.org/10.1002/app.12890>.
- [28] J. Chmelář, R. Pokorný, P. Schneider, K. Smolná, P. Bělský, J. Kosek, Free and constrained amorphous phases in polyethylene: interpretation of 1H NMR and SAXS data over a broad range of crystallinity, *Polymer* 58 (2015) 189–198, <https://doi.org/10.1016/j.polymer.2014.12.036>.
- [29] B. Goderis, H. Reynaers, R. Scherrenberg, V.B.F. Mathot, M.H.J. Koch, Temperature reversible transitions in linear polyethylene studied by TMDSC and time-resolved, temperature-modulated WAXD/SAXS, *Macromolecules* 34 (2001) 1779–1787, <https://doi.org/10.1021/ma001759y>.
- [30] I.G. Voigt-Martin, L. Mandelkern, Numerical analysis of lamellar thickness distributions, *J. Polym. Sci., Part B: Polym. Phys.* 27 (1989) 967–991, <https://doi.org/10.1002/polb.1989.090270502>.
- [31] C.G. Vonk, A.P. Pijpers, X-ray diffraction study of nonlinear polyethylene: I. Room-temperature observations, *J. Polym. Sci. 2 Polym. Phys.* 23 (1984) 2517–2537, <https://doi.org/10.1002/pol.1985.180231210>.
- [32] N. Stribeck, Small-angle X-ray scattering functions in the vicinity of zero scattering angle with an application to polymer blends, *Macromolecules* 29 (1996) 7217–7220, <https://doi.org/10.1021/ma951656t>.
- [33] J. Che, C.R. Locker, S. Lee, G.C. Rutledge, B.S. Hsiao, A.H. Tsou, Plastic deformation of semicrystalline polyethylene by X-ray scattering: comparison with atomistic simulations, *Macromolecules* 46 (2013) 5279–5289, <https://doi.org/10.1021/ma4005007>.
- [34] C. Burger, H.W. Zhou, H. Wang, I. Sics, B.S. Hsiao, B. Chu, L. Graham, M. J. Glimcher, Lateral packing of mineral crystals in bone collagen fibrils, *Biophys. J.* 95 (2008), <https://doi.org/10.1529/biophysj.107.128355>, 1985–1992.
- [35] R. Brämer, C. Gerdes, W. Wenig, Analysis of the small-angle X-ray scattering of linear polyethylene by a paracrystalline lattice model, *Colloid Polym. Sci.* 261 (1983) 293–298, <https://doi.org/10.1007/BF01413934>.
- [36] R. Brämer, Eindimensionale röntgenkleinwinkelstreuungsmeln parakristalliner lamellenclusterstrukturen, *Kolloid-Z. Z. Polym.* 250 (1972) 1034–1038, <https://doi.org/10.1007/BF01498885>.
- [37] W. Ruland, B. Smarsly, SAXS of self-assembled oriented lamellar nano-composite films: an advanced method of evaluation, *J. Appl. Crystallogr.* 37 (2004) 575–584, <https://doi.org/10.1107/S0021889804011288>.
- [38] G. Beaucage, D.W.W. Schaefer, Structural studies of complex systems using small-angle scattering: a unified Guinier/power-law approach, *J. Non-Cryst. Solids* 172–174 (1994) 797–805, [https://doi.org/10.1016/0022-3093\(94\)90581-9](https://doi.org/10.1016/0022-3093(94)90581-9).
- [39] G. Beaucage, Approximations leading to a unified exponential/power-law approach to small-angle scattering, *J. Appl. Crystallogr.* 28 (1995) 717–728, <https://doi.org/10.1107/S0021889895005292>.

- [40] G. Beaucage, Small-angle scattering from polymeric mass fractals of arbitrary mass-fractal dimension, *J. Appl. Crystallogr.* 29 (1996) 134–146, <https://doi.org/10.1107/S0021889895011605>.
- [41] K. Vogtt, G. Beaucage, M. Weaver, H. Jiang, Thermodynamic stability of worm-like micelle solutions, *Soft Matter* 13 (2017) 6068–6078, <https://doi.org/10.1039/c7sm01132f>.
- [42] G. Beaucage, J.H. Aubert, R.R. Lagasse, D.W. Schaefer, T.P. Rieker, P. Erlich, R. S. Stein, S. Kulkarni, P.D. Whaley, Nano-structured, semicrystalline polymer foams, *J. Polym. Sci., Part B: Polym. Phys.* 34 (1996) 3063–3072, [https://doi.org/10.1002/\(SICI\)1099-0488\(199612\)34:17<3063::AID-POLB18>3.0.CO;2-5](https://doi.org/10.1002/(SICI)1099-0488(199612)34:17<3063::AID-POLB18>3.0.CO;2-5).
- [43] P.D. Condo, E.J. Colman, P. Ehrlich, Phase equilibria of linear polyethylene with supercritical propane, *Macromolecules* 25 (1992) 750–753, <https://doi.org/10.1021/ma00028a038>.
- [44] A. Guinier, G. Fournet, *Small Angle Scattering of X-rays*, John Wiley & Sons, New York, US, 1955.
- [45] B.B. Mandelbrot, *The Fractal Geometry of Nature*, W. H. Freeman & Company, New York, US, 1983.
- [46] A. Mcglasson, K. Rishi, G. Beaucage, M. Chauby, V. Kuppa, J. Ilavsky, M. Rackaitis, Quantification of dispersion for weakly and strongly correlated nanofillers in polymer nanocomposites, *Macromolecules* 53 (2020) 2235–2248, <https://doi.org/10.1021/acs.macromol.9b02429>.
- [47] G. Porod, General theory, in: O. Glatter, O. Kratky (Eds.), *Small Angle X-Ray Scatt.*, Academic Press Inc., New York, US, 1982, pp. 17–51.
- [48] R.-J. Roe, *Methods of X-Ray and Neutron Scattering in Polymer Science*, Oxford university press, New York, US, 2000.
- [49] B. Crist, F.M. Mirabella, Crystal thickness distributions from melting homopolymers or random copolymers, *J. Polym. Sci., Part B: Polym. Phys.* 37 (1999) 3131–3140, [https://doi.org/10.1002/\(SICI\)1099-0488\(19991101\)37:21<3131::AID-POLB22>3.0.CO;2-M](https://doi.org/10.1002/(SICI)1099-0488(19991101)37:21<3131::AID-POLB22>3.0.CO;2-M).
- [50] Y. Furushima, M. Nakada, M. Murakami, T. Yamane, A. Toda, C. Schick, Method for calculation of the lamellar thickness distribution of not-reorganized linear polyethylene using fast scanning calorimetry in heating, *Macromolecules* 48 (2015) 8831–8837, <https://doi.org/10.1021/acs.macromol.5b02278>.
- [51] J.D. Hoffman, J.I. Lauritzen, Crystallization of bulk polymers with chain folding: theory of growth of lamellar spherulites, *J. Res. Natl. Bur. Stand. Sect. A Phys. Chem.* 65A (1961) 297, <https://doi.org/10.6028/jres.065a.035>.
- [52] R. Shroff, A. Prasad, C. Lee, Effect of molecular structure on rheological and crystallization properties of polyethylenes, *J. Polym. Sci., Part B: Polym. Phys.* 34 (1996) 2317–2333, [https://doi.org/10.1002/\(SICI\)1099-0488\(199610\)34:14<2317::AID-POLB3>3.0.CO;2-T](https://doi.org/10.1002/(SICI)1099-0488(199610)34:14<2317::AID-POLB3>3.0.CO;2-T).
- [53] D.H.S. Ramkumar, J.M. Caruthers, H. Mavridis, R. Shroff, Computation of the linear viscoelastic relaxation spectrum from experimental data, *J. Appl. Polym. Sci.* 64 (1997) 2177–2189, [https://doi.org/10.1002/\(sici\)1097-4628\(19970613\)64:11<2177::aid-app14>3.3.co;2-l](https://doi.org/10.1002/(sici)1097-4628(19970613)64:11<2177::aid-app14>3.3.co;2-l).
- [54] A. Prasad, R. Shroff, S. Rane, G. Beaucage, Morphological study of HDPE blown films by SAXS, SEM and TEM: a relationship between the melt elasticity parameter and lamellae orientation, *Polymer* 42 (2001) 3103–3113, [https://doi.org/10.1016/S0032-3861\(00\)00612-1](https://doi.org/10.1016/S0032-3861(00)00612-1).
- [55] H.D. Keith, F.J. Padden, A phenomenological theory of spherulitic crystallization, *J. Appl. Phys.* 34 (1963) 2409–2421, <https://doi.org/10.1063/1.1702757>.
- [56] H.D. Keith, F.J. Padden, Spherulitic crystallization from the melt. I. Fractionation and impurity segregation and their influence on crystalline morphology, *J. Appl. Phys.* 35 (1964) 1270–1285, <https://doi.org/10.1063/1.1713606>.
- [57] H.D. Keith, F.J. Padden, Spherulitic crystallization from the melt. II. Influence of fractionation and impurity segregation on the kinetics of crystallization, *J. Appl. Phys.* 35 (1964) 1286–1296, <https://doi.org/10.1063/1.1713607>.
- [58] P.J. Jenkins, A.M. Donald, The influence of amylose on starch granule structure, *Int. J. Biol. Macromol.* 17 (1995) 315–321, [https://doi.org/10.1016/0141-8130\(96\)81838-1](https://doi.org/10.1016/0141-8130(96)81838-1).
- [59] E.L. Heeley, D.J. Hughes, P.G. Taylor, A.R. Bassindale, Crystallization and morphology development in polyethylene-octakis(n-octadecyldimethylsiloxy) octasilsequioxane nanocomposite blends, *RSC Adv.* 5 (2015) 34709–34719, <https://doi.org/10.1039/C5RA03267A>.
- [60] F. Auriemma, C. De Rosa, M. Scoti, R. Di Girolamo, A. Malafronte, N.G. Galotto, Structural investigation at nanometric length scale of ethylene/1-octene multiblock copolymers from chain-shuttling technology, *Macromolecules* 51 (2018) 9613–9625, <https://doi.org/10.1021/acs.macromol.8b01947>.
- [61] G. Beaucage, H.K. Kammler, S.E. Pratsinis, Particle size distributions from small-angle scattering using global scattering functions, *J. Appl. Crystallogr.* 37 (2004) 523–535, <https://doi.org/10.1107/S0021889804008969>.
- [62] C.G. Vonk, The determination of the lamellar thickness in semi-crystalline polymers by small-angle scattering, *Makromol. Chem. Macromol. Symp.* 15 (1988) 215–222, <https://doi.org/10.1002/masy.19880150116>.
- [63] R.E. Cameron, A.M. Donald, A small-angle X-ray scattering study of the absorption of water into the starch granule, *Carbohydr. Res.* 244 (1993) 225–236, [https://doi.org/10.1016/0008-6215\(83\)85003-4](https://doi.org/10.1016/0008-6215(83)85003-4).
- [64] B. Crist, Analysis of small-angle X-ray scattering patterns, *J. Macromol. Sci. Part B* 39 (2000) 493–518, <https://doi.org/10.1081/MB-100100401>.